Domain morphology and mechanics of the H/T′ transition metal dichalcogenide monolayers

Joel Berry,[1,2] Songsong Zhou,[1] Jian Han,[1] David J. Srolovitz,[1,3,4] and Mikko P. Haataja[2,5,6]

[1]*Department of Materials Science and Engineering, University of Pennsylvania, Philadelphia, Pennsylvania 19104, USA*
[2]*Department of Mechanical and Aerospace Engineering, Princeton University, Princeton, New Jersey 08544, USA*
[3]*Department of Mechanical Engineering and Applied Mechanics, University of Pennsylvania, Philadelphia, Pennsylvania 19104, USA*
[4]*Department of Materials Science and Engineering, City University of Hong Kong, Hong Kong SAR, People's Republic of China*
[5]*Princeton Institute for the Science and Technology of Materials (PRISM), Princeton University, Princeton, New Jersey 08544, USA*
[6]*Program in Applied and Computational Mathematics (PACM), Princeton University, Princeton, New Jersey 08544, USA*

(Received 4 July 2018; revised manuscript received 14 September 2018; published 5 November 2018)

The properties of two-dimensional (2D) transition metal dichalcogenide (TMD) monolayers can be dynamically controlled via strain-induced displacive structural transformations between semiconducting (H) and metallic or semimetallic (T′) crystal structures. The shapes, symmetries, and kinetics of crystalline domains generated during these transformations and the mechanical response of transforming monolayers are of fundamental and applied interest in, e.g., phase change memory devices and the study of topologically protected edge states in quantum spin Hall insulating T′ crystals. We quantitatively characterize T′ domain morphologies during H → T′ transformations in both flat and bendable TMD monolayers using a combination of first principles and continuum calculations. Wulff constructions for $MoTe_2$ and MoS_2 show that T′ domains within much larger T′ domains are either rhombi of fixed proportions (if nonmisfitting) or rectangles whose aspect ratio A_R increases with domain size L_0 (if misfitting). Isolated T′ domains within much larger H domains undergo a morphological crossover from compact to elongated shapes at $L_0 \approx$ 100–200 nm if the sheet is constrained to be flat or $L_0 \gtrsim 2$ μm if the sheet is free to bend. This crossover is driven by a competition between anisotropic interfacial energy and elastic misfit energy, and its position can be tuned via the monolayer-substrate interaction strength. It is shown that the aspect ratio A_R obeys a scaling law $A_R \sim L_0^{2/3}$. Stress-strain response characterized as a function of strain orientation reveals extreme anisotropy in the effective elastic modulus through H/T′ coexistence. Ferroelastic multidomain T′-WTe_2 monolayers are found to exhibit two to three regimes of reversible mechanical response, and localized buckling in freely suspended T′ monolayers is shown to qualitatively alter T′ domain symmetries.

DOI: 10.1103/PhysRevMaterials.2.114002

I. INTRODUCTION

The electronic and optical properties of many two-dimensional (2D) materials vary qualitatively with strain state [1,2] and with crystal structure/phase [3]. With the ability to controllably tune phase and strain state, there are many interesting opportunities for employing 2D materials in novel devices and applications. Properties of 2D transition metal dichalcogenide (TMD) monolayers can be dynamically and locally varied via strain-induced [4–10] or electrostatically-induced [9,11,12] displacive structural transformations, permitting rapid and possibly reversible switching between the semiconducting (H) and metallic or semimetallic (T′) crystal structures. The search for and exploitation of topologically protected edge states in T′ TMDs, which are large-gap quantum spin Hall insulators [13], is also facilitated by the ability to control T′ domain morphology and to realize atomically sharp T′ edges or particular coherent interfaces with other crystalline domains (H or differently-oriented T′) [14].

First-principles calculations have revealed that the thermodynamic equilibrium state can be switched between the H and T′ phases with application of mechanical strain [4]. The uniaxial strain required to induce transformation in $MoTe_2$ is particularly small, of order 1–2%. Atomic force microscope tip-induced H → T′ transformations have since been reported in $MoTe_2$ multilayers [5]. Exploitation of this transformation in devices relies on the ability to predict and control T′ domain patterns. We have recently demonstrated through numerical simulations that the H → T′ transformation is characterized by complex, strain orientation-dependent multidomain H-T′ microstructures [10]. The resulting T′ monolayer also exhibits a multidomain T′ variant microstructure composed of characteristic, scale-independent geometric patterns that result from strain accommodation. Strategies for systematic control of crystal structure domain morphologies and generation of functionally patterned conductive T′ domains have been proposed based on application of spatially modulated strains through local probes and/or patterned substrates [10]. Monolayers with this functionality constitute dynamically programmable electromechanical 2D materials, in which localized conducting regions can be dynamically patterned in an otherwise semiconducting TMD monolayer. Related heterostructures are also of interest for advanced electronic device [15], ferroelastic and shape memory [8], hydrogen evolution catalysis [16], phase change memory [7,9], and Ohmic contact [17–19] applications.

Here, we employ a combination of first principles calculations and continuum field theory simulations to quantitatively characterize T′ domain morphologies during H → T′ transformations in both flat and bendable TMD monolayers. The

remainder of the paper is organized as follows. In Sec. II, the first principles methods and continuum model employed in later sections are first outlined. In Sec. III, the results of energy minimization calculations for T′ domains under various conditions are presented. The energy minimizing domain shapes are found to be controlled by a competition between anisotropic interfacial energy and elastic misfit energy. This competition leads to a crossover from compact faceted shapes to elongated needlelike shapes above a critical domain size, followed by a scaling regime in which aspect ratio increases as $A_R \sim L_0^{2/3}$.

Both monolayers strongly bound to a flat substrate and freely suspended monolayers exhibit qualitative changes in T′ domain shape with increasing domain size, but the crossover to highly elongated shapes in freely suspended monolayers can be strongly suppressed by the effects of buckling. The strength of the monolayer-substrate coupling can therefore be employed as a means of controlling T′ domain geometry in partially-transformed monolayers.

In Sec. IV, we characterize the stress-strain response during strain-induced transformations as a function of strain orientation, as well as features of the mechanical response of ferroelastic multidomain T′-WTe_2 sheets. The effective elastic modulus of the monolayer is shown to vary dramatically and systematically with the nature of the applied strain in regions of H/T′ coexistence. Freely suspended ferroelastic T′-WTe_2 monolayers are found to exhibit either two or three regimes of elastic stress-strain response, depending on the nature of the applied strain. Localized buckling in freely suspended T′ monolayers is also shown to qualitatively alter T′ domain symmetries. We conclude with a brief discussion of potential applications.

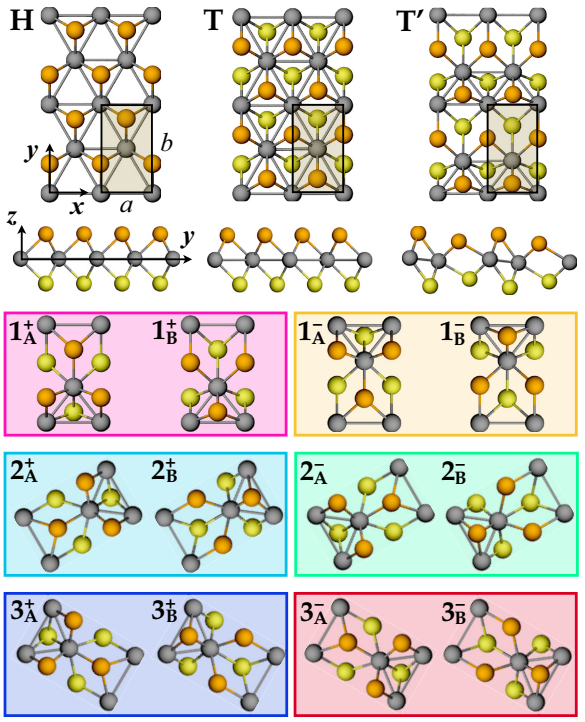

FIG. 1. Upper: TMD crystal structures. The flat sheet lies in the (x, y) plane. Metal and upper/lower chalcogen atoms are shown in gray and orange/yellow, respectively. Lower: 12 T′ orientational variants as viewed in the (x, y) plane, and their designations $p^{\pm}_{\alpha}$; $p \in \{1, 2, 3\}$, superscripts $(\pm)$, and subscripts $\alpha \in \{A, B\}$ distinguish between orientation, direction of dimerization, and direction of x-y mirror asymmetry, respectively. Colored boxes indicate the scheme employed for simulation visualization.

II. METHODS

Monolayer TMDs of the MX_2 type contain three atomic layers, with transition metal atoms M occupying the central layer and chalcogen atoms X occupying the two outer layers. Monolayer TMDs exhibit crystal structures with trigonal prismatic (H), octahedral (T), or distorted octahedral (T′) symmetry [Fig. 1(a)]. In the absence of a lattice distortive transformation strain, perfect H and T structures can be interchanged by simple displacements of a single X layer along $[0, \sqrt{3}/3]a$, $[-1, -\sqrt{3}/3]a/2$, or $[1, -\sqrt{3}/3]a/2$ (Fig. 1). These modify the XMX stacking sequence from βAβ (H) to βAγ (T) or γAβ (T), where A and β/γ indicate the structure of the M layer and upper and lower X layers, respectively. The appropriate symmetry-lowering distortions of the T lattice generate the T′ lattice with dimerized metal atoms. Symmetry permits twelve possible orientations/variants of the T′ unit cell relative to the initial (fixed) H unit cell, as shown in Fig. 1(a). These include three primary orientations ($p \in \{1, 2, 3\}$), each with four subvariants resulting from dimerization and stacking asymmetries.

First-principles calculations have shown that the T phase in monolayer TMDs is dynamically unstable (possesses an imaginary phonon mode) in the absence of external stabilizing influences [4,20,21]. The T phase has been observed in experiments on some TMD monolayers where exfoliation and/or structural transformation is induced by chemical processes involving a charge transfer mechanism (e.g., lithiation or adsorbate effects) that externally stabilizes the otherwise unstable T phase [3,15,17,21,22].

A. First principles calculations

To inform our study of H/T′ domain morphology and its relation to mechanics, we first determined the energies of the primary H/T′ and T′/T′ interfaces in $MoTe_2$ and MoS_2 using density functional theory (DFT) calculations. These calculations were performed using the Vienna *ab initio* simulation package (VASP) using a plane-wave basis set [23,24] and the projector augmented wave method [25]. The generalized gradient approximation [26] with the Perdew-Burke-Ernzerhof functional [27] was employed to treat exchange-correlation effects. The T′/T′ and H/T′ interface energies for $MoTe_2$ and MoS_2 were calculated for several misorientations and inclination angles within supercells containing two parallel interfaces. All systems were fully relaxed until the total force on each atom was less than 0.01 eV/Å. A vacuum layer of minimum thickness of 20 Å perpendicular to the monolayer was employed to minimize interactions between the monolayer and its periodic images. The kinetic energy cutoff was set to 420 eV. The Γ-centered k-point grid up to $12 \times 1 \times 1$ was employed in Brillouin zone integration.

Interfacial energies were determined by subtracting the H and/or T′ bulk energy contributions from the total energy of the periodic supercell and assigning the rest to the interfaces. Because of the inversion symmetry of the T′ structure, any two T′/T′ interfaces in our periodic supercell are identical; the absence of this symmetry in the H phase implies that any two H/T′ interfaces within our supercell are not identical. The computed H/T′ interface energies therefore correspond to the average of those of the two nonidentical H/T′ interfaces. See Refs. [10] and [28] for more details.

Interfaces between elastically misfitting domains possess special preferred inclinations if the axial transformation strains along the two principal strain axes have opposite sign. These special inclinations (i.e., habits) are those at which the elastic energy of an infinitely long and narrow daughter domain embedded within a homogeneous parent matrix vanishes. A proliferation of needlelike domains oriented along the habit inclinations is thus expected when the morphology is dominated by elastic energy. However, the H/T′ interfacial energies at these inclinations (41.78° for $MoTe_2$ and 10.34° for MoS_2) are computationally inaccessible due to the large supercell sizes required. We therefore instead use calculated energies at nearby (40.89° and 10.89°) inclinations for which the required supercell sizes are tractable [see Fig. 4(b)].

B. Continuum model

To study microstructure evolution and the mechanical response of bendable H/T′ monolayers, interface energies and other quantities computed from first principles are directly incorporated into a continuum phase-field microelasticity (PFM) model as input parameters. This model was introduced in Ref. [10]; here we summarize its essential features and governing equations. [See Appendix A for details.]

PFM models incorporate the effects of transformation strain, coherent crystal-crystal interfaces, long-range elastic interactions between misfitting domains, and coupling to applied strain [29–31]. The TMD monolayer in our formulation is treated as a thin, bendable elastic plate in which an effectively 2D crystal symmetry change is induced by strain. Unlike earlier PFM applications, our description includes the effect of out-of-plane deformation $w(\vec{r})$ and the bending energy f_{bend}, described within the large deflection theory of plates framework (e.g., see Ref. [32]). In the limit $w \to 0$, our model reduces to earlier 2D hexagonal → orthorhombic transformation models [33–36].

A free energy functional F_{tot} for the structurally inhomogeneous monolayer contains separate chemical and elastic contributions

$$F_{\text{tot}} = \int_A (f_{\text{chem}} + f_{\text{elas}}) dA, \tag{1}$$

where

$$f_{\text{chem}} = h f_{\text{bulk}}(\eta_p) + \frac{h}{2} \sum_p |\beta(\phi) \nabla \eta_p|^2 \tag{2}$$

is the stress-free energy density of the structurally inhomogeneous monolayer, h is the monolayer thickness, and f_{elas} contains all self and elastic interaction energy densities associated with the arbitrary configuration of structural domains within the monolayer. These terms are both functions of the order parameter fields $\eta_p(\vec{r})$, which distinguish the different T′ variants and the H structure. In the following, $\eta_p(\vec{r})$ is normalized by its maximum or equilibrium value η_0, such that it only assumes values between zero and one. $\beta(\phi)$ is proportional to interfacial energy and may vary with interface inclination angle ϕ. Its form is parameterized according to the results of our DFT calculations presented in Sec. III C.

The form of $f_{\text{bulk}}(\eta_p)$ should in principle contain all terms allowed by the H phase symmetry and the order of the transformation, up to an order determined by the target accuracy [33–36]. We employ a slightly simplified formulation here that describes six T′ variants, two at each of the three orientations, in terms of three η_p fields. Elastic strains associated with the three T′ orientations are thus captured, and among the four possible strain-equivalent or antiphase T′ variants at each orientation, we distinguish between opposing T′ dimerization directions, p^+ and p^-, but not p_{A} and p_{B} stacking variants [Fig. 1(a)]. Values $\eta_p = -1$ and 1 thus represent p^- and p^+ domains, respectively, while regions where all $\eta_p = 0$ correspond to H domains. This simplification allows the general morphologies of the secondary antiphase domain structures to be characterized without the full complexity of a 12 variant description and has no significant effect on the elastic fields that drive the transformation and its primary morphology.

Following [33–36], we focus on the regime in which elastic strain energy (rather than bulk chemical energy) dominates microstructural domain patterns; the main features of the results are unaffected by the detailed form of f_{bulk}. This allows use of a simplified form of the bulk free energy that neglects odd powers in η_p and reflects the basic symmetries of rotational invariance and equivalence between + and − variants as defined in Fig. 1 [$f_{\text{bulk}}(\eta_1 = \pm 1, \eta_2 = 0, \eta_3 = 0) = f_{\text{bulk}}(\eta_1 = 0, \eta_2 = \pm 1, \eta_3 = 0) = f_{\text{bulk}}(\eta_1 = 0, \eta_2 = 0, \eta_3 = \pm 1)$]. It is

$$f_{\text{bulk}} = \Delta f(T) \left[\frac{a}{2} \sum_p \eta_p^2 - \frac{b}{4} \sum_p \eta_p^4 + \frac{c}{6} \left(\sum_p \eta_p^2 \right)^3 \right], \tag{3}$$

where $\Delta f(T)$ and the adjustable constants a, b, and c set the magnitude of the chemical driving force for transformation.

The elastic energy density (energy/area) of the thin elastic plate is divided into stretching and bending contributions,

$$f_{\text{elas}} = h f_{\text{stretch}} + f_{\text{bend}}. \tag{4}$$

The stretch or in-plane component can be expressed in general form as

$$f_{\text{stretch}} = \frac{1}{2} \lambda_{ijkl} \epsilon_{ij} \epsilon_{kl} + \sum_p \left[\frac{1}{2} \lambda_{ijkl} \epsilon_{ij}^0(p) \epsilon_{kl}^0(p) \eta_p^4 - \lambda_{ijkl} \epsilon_{ij} \epsilon_{kl}^0(p) \eta_p^2 \right], \tag{5}$$

where λ_{ijkl} is the elastic stiffness tensor, $\epsilon_{ij}^0(p) = \mathbf{R}[\theta_p] \epsilon_{ij}^0 \mathbf{R}^{\mathbf{T}}[\theta_p]$ is the transformation strain tensor of variant

p, and

$$\epsilon_{ij}(\vec{r}) = \bar{\epsilon}_{ij} + \tfrac{1}{2}(u_{i,j} + u_{j,i} + w_{,i}w_{,j}) \tag{6}$$

is the elastic strain tensor appropriate for large out-of-plane deflections ($i, j, k, l = x, y$). The Einstein summation convention is used throughout this paper, and partial derivatives are represented by commas in the subscripts, e.g., $\partial w/\partial r_i \rightarrow w_{,i}$, $\partial u_i/\partial r_j \rightarrow u_{i,j}$, and $\partial^2 w/\partial r_i \partial r_j \rightarrow w_{,ij}$. $\mathbf{R}[\theta_p]$ is the 2D rotation matrix, $\epsilon^0_{xx} = (a_{T'} - a_H)/a_H$, $\epsilon^0_{yy} = (b_{T'} - b_H)/b_H$, $\epsilon^0_{xy} = 0$, $\theta_1 = 0$, $\theta_2 = 2\pi/3$, and $\theta_3 = -2\pi/3$. u_i are in-plane displacements, w denotes out-of-plane displacement, and $\bar{\epsilon}_{ij}$ is the applied macroscopic strain.

The bending energy of an elastically isotropic thin plate is

$$f_{\text{bend}} = \frac{\kappa}{2}\{(\nabla^2 w)^2 + 2(1-\nu)[(w_{,xy})^2 - w_{,xx}w_{,yy}]\}, \tag{7}$$

where the bending modulus is $\kappa = \mu h^3/6(1-\nu)$, and μ and ν are the shear modulus and Poisson's ratio, respectively. For isotropic solids under plane stress, the elastic constant tensor reduces to

$$\lambda_{ijkl} = \mu\left(\delta_{ik}\delta_{jl} + \delta_{il}\delta_{jk} + \frac{2\nu}{1-\nu}\delta_{ij}\delta_{kl}\right), \tag{8}$$

where δ_{ij} is the Kronecker delta, such that the elastic Green's function is

$$G_{ij}(\vec{k}) = \frac{\delta_{ij}}{\mu k^2} - \frac{(1+\nu)k_i k_j}{2\mu k^4}, \tag{9}$$

where $\vec{k}$ is wave vector and $k^2 = k_x^2 + k_y^2$.

In group VI TMD monolayers, the parent H phase is elastically isotropic (to a very good approximation) [37–40], while the daughter T′ phase is anisotropic (typically ∼20–30% softer along a than along b [39–41]). Nonetheless, in this analysis, we neglect the small elastic anisotropy and the elastic heterogeneity in the sheet and choose a single set of elastic constants for the entire sheet (this greatly simplifies the calculations and the theoretical analysis presented below). We describe the elastic constants of the entire sheet to match that of the parent phase; this assumption is most accurate when the area fraction of the T′ phase is small and/or when microstructure evolution is dominated by interfacial rather than elastic energies. One or both of these conditions is satisfied in most of the results discussed below; we implicitly assume that, when they are not, the elastic asymmetry effects will not significantly alter the main features of results. Further study is required to quantify the effects of T′ anisotropy. A formulation applicable to elastically heterogeneous and anisotropic systems will be examined in a forthcoming work.

The equations of mechanical equilibrium for in-plane displacements $u_i(\vec{r})$, out-of-plane displacements $w(\vec{r})$, and order parameters $\eta_p(\vec{r})$ are derived in Appendix A. The incorporation of out-of-plane displacement w and bending energy f_{bend} modifies the conditions of equilibrium such that a tractable closed-form solution in terms of the order parameters η_p alone cannot be obtained. Instead, we have a closed set of coupled, nonlinear mesoscale governing equations for each of the fields, $u_i(\vec{r})$, $w(\vec{r})$, and $\eta_p(\vec{r})$:

$$\lambda_{ijkl}k_j k_k \hat{u}_l(\vec{k}) = -i\sum_{p=1}^{v}\sigma^0_{ij}(p)k_j\hat{\eta^2_p}(\vec{k}) + \lambda_{ijkl}\hat{N}_{jkl}(\vec{k}), \tag{10}$$

$$\sum_{p=1}^{v}\sigma^0_{ij}(p)\left[\left(\eta^2_p\right)_{,j}w_{,i} + \eta^2_p w_{,ij}\right] + \kappa\nabla^4 w - \frac{1}{2}\lambda_{ijkl}[(2u_{k,l}w_{,j} + w_{,j}w_{,k}w_{,l})_{,i} + 2\bar{\epsilon}_{kl}w_{,ij}] = 0, \tag{11}$$

$$2\lambda_{ijkl}\epsilon^0_{kl}(p)\eta_p\left[\epsilon^0_{ij}(p)\eta^2_p - \epsilon_{ij}(\vec{r})\right] + \frac{\delta f_{\text{chem}}}{\delta\eta_p} = 0, \tag{12}$$

where k is wave number, $\hat{u}_i(\vec{k})$ is the Fourier transform of $u_i(\vec{r})$, $\hat{\eta^2_p}(\vec{k})$ is the Fourier transform of $\eta^2_p(\vec{r})$, and

$$\hat{N}_{jkl}(\vec{k}) = \int_A w_{,k}w_{,jl}e^{-i\vec{k}\cdot\vec{r}}dA. \tag{13}$$

Equation (10) can be solved analytically to determine the in-plane displacement fields

$$\hat{u}_i(\vec{k}) = -i\sum_p G_{ij}(\vec{k})\sigma^0_{jk}(p)k_k\hat{\eta^2_p}(\vec{k}) + G_{ij}(\vec{k})\lambda_{jklm}\hat{N}_{klm}(\vec{k}), \tag{14}$$

where $G_{ij}(\vec{k}) = \Omega_{ij}(\vec{n})/k^2$, $\Omega^{-1}_{ij}(\vec{n}) = \lambda_{iklj}n_k n_l$, and $\vec{n} = \vec{k}/|k|$ [see Eq. (9) for the isotropic case]. However, Eqs. (11) and (12) are nonlinear with nonconstant coefficients. w and η_p are therefore numerically iterated to mechanical equilibrium using physically-motivated evolution equations.

Out-of-plane displacements in thin elastic sheets are mediated by flexural phonons which relax/damp out over some characteristic time. Similarly, coherent η_p interfaces can, in principle, move displacively at speeds near those of in-plane phonons (which are also damped over time). We therefore employ simple, physically-motivated, but phenomenological, evolution equations that approximate such kinetic processes by iterating to mechanical equilibrium by identical small increments of time t:

$$w_{,tt} + (\gamma_{0w} - \gamma_{1w}\nabla^2)w_{,t} = -\alpha^2_w\frac{\delta\tilde{F}_{\text{tot}}}{\delta w} + \nu_w \tag{15}$$

$$\eta_{p,tt} + (\gamma_{0p} - \gamma_{1p}\nabla^2)\eta_{p,t} = -\alpha^2_p\frac{\delta\tilde{F}_{\text{tot}}}{\delta\eta_p} + \nu_p, \tag{16}$$

where $\tilde{F}_{\text{tot}} = F_{\text{tot}}/k_B T$. These damped wave equations incorporate both rapid propagating waves of displacement (quasiphonons) and slow overdamped relaxations. γ_{0i} is a uniform damping parameter, γ_{1i} is a damping parameter that preferentially suppresses large wave-number oscillations, and α_i is the wave speed. ν_i is Gaussian noise that is delta correlated in space and time, i.e., $\langle\nu_i\rangle = 0$ and $\langle\nu_i(\vec{r},t)\nu_i(\vec{r}',t')\rangle = -2k_B T\delta(\vec{r}-\vec{r}')\delta(t-t')$. These types of evolution equations [Eqs. (15) and (16)] have been widely used in phase field modeling (e.g., to describe rapid solidification processes [42–44] and transport phenomena in solids driven by both long range elastic interactions (phonons) and diffusion [45]) and can be derived from microscopic considerations (e.g., as the hydrodynamic evolution equation for mass density in isothermal solids [46]). However, since the main focus of the

present study is the determination of relaxed microstructures rather than phonon dynamics, Eqs. (15) and (16) can also be viewed as a numerical approach to relaxing the systems to free energy minima (although there is no guarantee that the resultant structures correspond to a global free energy minimum).

Equation (15) describes the propagation and damping of transverse out-of-plane waves, analogous to flexural acoustic (ZA) phonons. However, use of the exact solutions for u_x and u_y [Eq. (14)] bypasses the incorporation of longitudinal and transverse in-plane acoustic phonons, LA and TA, respectively. This approximation can be justified when LA and TA modes relax much faster than ZA modes. Such a separation of scales is a reasonable physical approximation for TMD monolayers at the length scales described by our continuum model since the in-plane elastic moduli are large and the bending moduli are small, leading to LA and TA wave speeds [47] that are at least ∼6 times greater than the effective ZA wave speeds for wavelengths $\lambda \gtrsim 16a \simeq 5$ nm [48]. For simulations in which physically-motivated η_p kinetics are not required (e.g., when only equilibrium states are of interest), we employ the purely dissipative scheme outlined in Appendix B rather than Eq. (16).

Details of the numerical methods used to solve Eqs. (10)–(12), (15), and (16) are provided in Ref. [10]. $\Delta f = 312$ meV/Å^3, $h = 0.65$ nm, and $\kappa = 10$ eV are used in all simulations, and those with bending employ $\gamma_{0w} = 50$/s, $\gamma_{1w} = 2 \times 10^{-19}$ m^2/s, and $\alpha_w = 100$ m/s. The latter value is an estimate of typical wave speeds for ∼5–500 nm ZA phonons in TMD monolayers [49]. In Sec. III, η_p are evolved using Eq. (B1) with $M_p = 1$ /s, and H/T′ interfacial anisotropy is implemented via $\beta(\hat{\phi}) = \bar{\beta}\{2 + \epsilon[\cos(4\hat{\phi} - \pi) + \cos(6\hat{\phi})]\}/2$ with $\bar{\beta} = 167$ (meV/Å)$^{1/2}$ and $\epsilon = 0.215$. $\hat{\phi}$ denotes the direction normal to the interface inclination ϕ. The relation $\gamma^{\mathrm{H0T'}}(\hat{\phi}) = h\sqrt{W}\beta(\hat{\phi})$ sets the value of $\bar{\beta}$, where $W = (b-d)(8ac + bd - b^2)\Delta f/54c^2$ and $d = \sqrt{b^2 - 4ac}$. In Sec. IV, η_p are evolved using Eq. (16) with $\gamma_{0p} = 500$/s, $\gamma_{1p} = 2 \times 10^{-18}$ m^2/s, and $\alpha_p = 1000$ m/s (an estimate of typical wave speeds for LA phonons $\gtrsim$10 nm in TMD monolayers [49]) and interfacial anisotropy is neglected with $\epsilon = 0$.

Material parameters for $MoTe_2$ are $\epsilon^0_{xx} = -0.0299$ [10], $\epsilon^0_{yy} = 0.0374$ [10], $\mu = 50$ GPa [50], $\nu = 0.24$ [50], $a = 0.0031$, $b = 0.002$, $c = 0.00125$, and $\eta_0 = 1.14$. For WTe_2, we set $\epsilon^0_{xx} = -0.0172$ [4], $\epsilon^0_{yy} = 0.0270$ [4], $\mu = 57$ GPa [50], $\nu = 0.16$ [50], $a = -0.001$, $b = 0.002$, $c = 0.0021$, and $\eta_0 = 1.14$.

III. INTERFACE ENERGIES AND T′ DOMAIN MORPHOLOGIES

In this section, we report the $MoTe_2$ interface energies determined from DFT calculations. We also report T′ domain morphologies, determined through a combination of Wulff construction, continuum elastic analysis of transformation strain tensors, semianalytic Eshelby inclusion energy calculations (with anisotropic interfacial energies) and continuum model simulations. Similar results for MoS_2 are provided in Appendix C. We employ the notation AθB to denote an interface between phases A and B (and/or a domain of phase A embedded within a much larger domain of phase B) with A,B ∈ (H, T′) and where θ is the relative misorientation (in degrees) between A and B.

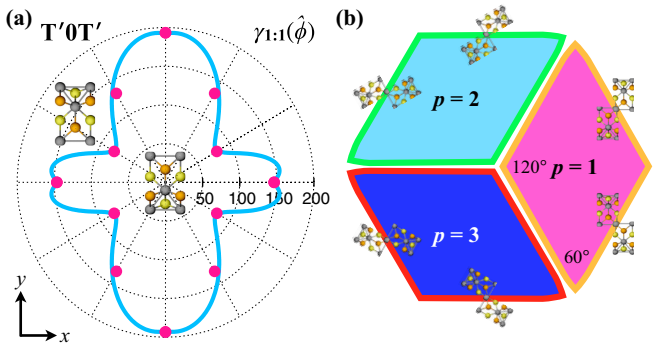

FIG. 2. T′0T′ interfaces and domain morphologies. (a) Anisotropic interfacial energy $\gamma_{1:1}(\hat{\phi})$ (meV/Å) as determined from DFT calculations (points) and the best fit to Eq. (17) (line). (b) Equilibrium (sub)domain shapes for each variant orientation p as determined from the Wulff construction employing the best fit to Eq. (17).

A. T′0T′ interfaces and domains

Coexisting domains of T′ variants with the same orientation but different secondary structure (T′0T′) have zero misfit strain. Two domains, $p^{\pm}_{\alpha}$ and $q^{\pm}_{\beta}$, with $p = q$ but $\alpha \neq \beta$ and/or different superscript ± fall into this category. Their morphology is therefore determined by the inclination dependence of the T′0T′ interfacial energy $\gamma_{p:p}(\hat{\phi})$ alone. This dependence, previously reported in Ref. [10], is shown in Fig. 2(a). Note that $\hat{\phi}$ denotes the direction normal to the interface inclination ϕ.

To perform a Wulff construction and determine the equilibrium shape of a T′0T′ domain, we must choose a functional form for $\gamma_{p:p}(\hat{\phi})$. Based on the dual twofold symmetry of the T′ lattice and the large anisotropy revealed by DFT calculations, we will assume that a global cusped minimum occurs at $\hat{\phi} = 30°$ and local minima at $\hat{\phi} = 0°$ and 90° from the a axis of variant p. We then write the interfacial energy as

$$\gamma_{p:p}(\hat{\phi}) = \begin{cases} \bar{\gamma}^{I}_{p:p}\left(1 + \epsilon^{I}_{p:p}\cos\left(C^{I} - \hat{\phi}\right)\right), & 0 \leqslant \hat{\phi} < 30° \\ \bar{\gamma}^{II}_{p:p}\left(1 + \epsilon^{II}_{p:p}\cos\left(\hat{\phi} - C^{II}\right)\right), & 30° \leqslant \hat{\phi} < 90° \end{cases}, \tag{17}$$

where $\bar{\gamma}^{I}_{p:p}$, $\bar{\gamma}^{II}_{p:p}$, $\epsilon^{I}_{p:p}$, $\epsilon^{II}_{p:p}$, C^{I}, and C^{II} are fitting parameters. The best fit to this functional form and the resulting Wulff construction are shown in Figs. 2(a) and 2(b). The equilibrium shape is nearly a rhombus composed of two equilateral triangles mirrored along one base. The orientation of the rhombus for each variant orientation is shown for completeness. These results are not particularly sensitive to the choice of functional form used in Eq. (17). The geometry of the Wulff construction requires, e.g., that $\gamma_{1:2}(0°) \leqslant 2\gamma_{1:2}(30°)/\sqrt{3}$ or $\gamma_{1:2}(90°) \leqslant 2\gamma_{1:2}(30°)$ for the domain shape to be influenced by the form of $\gamma_{1:2}$ near $\hat{\phi} = 0°$ and 90°, respectively. The computed values are above these thresholds; $\gamma_{1:2}(0°) \simeq 1.83\gamma_{1:2}(30°)$ and $\gamma_{1:2}(90°) \simeq 2.42\gamma_{1:2}(30°)$. The rhombic shape will only

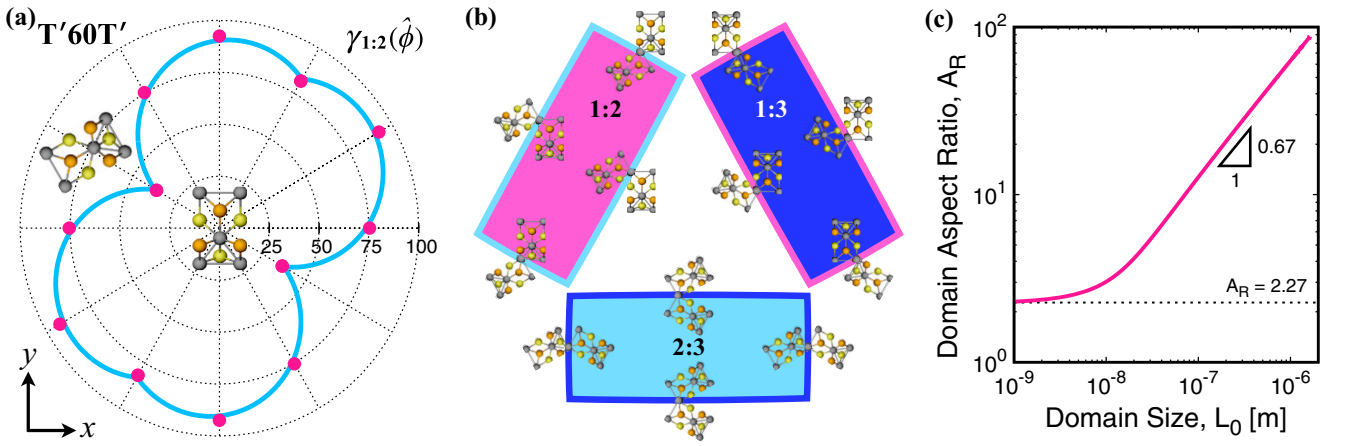

FIG. 3. T′60T′ interfaces and domain morphologies. (a) Anisotropy in interfacial energy $\gamma_{1:2}(\hat{\phi})$ as determined from DFT calculations (points) and the best fit to Eq. (18) (line). Energy units are meV/Å. (b) Equilibrium domain shapes for each variant orientation pair p:q as determined from the Wulff construction employing the best fit to Eq. (18), but neglecting the effect of misfit strain (valid only for very small domain sizes). The possible crystal orientations across each interface are shown for each pair; the inner:outer domains can be p:q or q:p. (c) Equilibrium domain axial ratio A_R increases with domain size L_0, crossing over from interface dominated to elastic misfit dominated A_R behavior above $L_0 \simeq 10$ nm. Results were obtained via the Eshelby misfitting inclusion calculation with anisotropic interfacial energy described in the main text.

be altered if interfacial energies at any of the unexamined inclinations are sufficiently near $\gamma_{1:2}(30^\circ)$.

B. T′60T′ interfaces and domains

Coexisting domains of T′ variants with different orientations (T′60T′, $p \neq q$) have nonzero misfit strain. Their morphology is therefore determined by a balance between the inclination dependence of the misfit strain accommodation and the inclination dependence of the T′60T′ interfacial energy $\gamma_{p:q}(\hat{\phi})$.

The inclination dependence of $\gamma_{p:q}(\hat{\phi})$, also previously reported in Ref. [10], is shown in Fig. 3(a). We propose a functional form for $\gamma_{p:q}(\hat{\phi})$ $(-30^\circ \leqslant \hat{\phi} < 60^\circ)$ that is consistent with dual twofold symmetry of the T′ lattice, having cusped minima at the inclination that bisects the b axes of variants p and q (as well as its normal):

$$\gamma_{p:q}(\hat{\phi}) = \bar{\gamma}_{p:q}(1 + \epsilon_{p:q}\cos(C - \hat{\phi})), \tag{18}$$

where $\bar{\gamma}_{p:q}$, $\epsilon_{p:q}$, and C again denote fitting parameters. The best fit to this functional form and the resulting Wulff construction (which neglects the effect of misfit strain) are shown in Figs. 3(a) and 3(b). The equilibrium shape of a T′ domain embedded within another infinite T′ domain of different orientation in the absence of misfit strain (valid only for very small domain sizes) is nearly rectangular. The long axis of the rectangle is aligned with the bisector of the b axes of p and q, and its axial or length to width ratio is $A_R \simeq 2.27$. These results are insensitive to the detailed functional form of $\gamma_{p:q}(\hat{\phi})$; the basic domain shape would only be altered if any interface energies are significantly smaller than those predicted by Eq. (18).

The above analysis is only applicable to very small embedded domains. A complete analysis requires consideration of misfit strain. A characterization of the T′ → T′ transformation strain tensors $\epsilon^0_{ij}(p{:}q)$ between T′ orientational variants p and $q \in \{1, 2, 3\}$ is shown in Table I for $\{\text{Mo,W}\}\{\text{S,Se,Te}\}_2$. The tensors for all three pairs in a given system are equivalent by symmetry. We denote the counterclockwise rotation from the $p = 1$ a axis that diagonalizes a given $\epsilon^0_{ij}(p{:}q)$ as $\psi_{p:q}$. The diagonalized $\epsilon^0_{ij}(p{:}q)$ is then defined from $\tilde{\epsilon}^0_{ij} = R^{-1}_{ij}[\psi_{p:q}]\epsilon^0_{ij}(p{:}q)R_{ij}[\psi_{p:q}]$ and has nonzero components $\tilde{\epsilon}^0_{xx}$ and $\tilde{\epsilon}^0_{yy}$ (independent of p and q). The T′ → T′ transformation strains are close to the pure shear limit ($\tilde{\epsilon}^0_{xx} = -\tilde{\epsilon}^0_{yy}$ or $\tilde{R} \ll 1$) in each system.

Table II shows the corresponding T′60T′ interface inclinations $\phi^{\text{int}}_{p:q}$ with lowest interfacial energy and the equilibrium habit inclinations $\phi^{\vec{n}}_{p:q}$ and $\phi^{\vec{l}}_{p:q}$ computed from each $\epsilon^0_{ij}(p{:}q)$. The elastic misfit energy and the interfacial energy are minimized at nearly the same interface orientations $\phi^{\text{int}}_{p:q} \simeq \phi^{\vec{n}}_{p:q}$. The second habit inclination $\phi^{\vec{l}}_{p:q}$ coincides with a larger interfacial energy and is therefore unfavorable. For pure shear misfit, the habit inclinations are $\pm 45^\circ$ from the orthogonal axes specified by $\psi_{p:q}$. Pure shear misfit would therefore result in habit inclinations $\phi^{\vec{n}}_{p:q} = \psi_{p:q} - 45^\circ$ and $\phi^{\vec{l}}_{p:q} = \psi_{p:q} + 45^\circ$. The computed values in Table II differ from this limit by less than 2°.

We therefore expect that T′-MX_2 systems will exhibit the interface inclinations $\phi^{\text{int}}_{p:q} \simeq \phi^{\vec{n}}_{p:q}$ given in Table II relative to the $p = 1$ a axis. These values agree with the preferred inclinations obtained from first principles [8]. In our PFM simulations, without interfacial anisotropy, both $\phi^{\vec{n}}_{p:q}$ and $\phi^{\vec{l}}_{p:q}$ are observed with equal probability, as expected. However, with interfacial anisotropy the higher energy interfaces at $\phi^{\vec{l}}_{p:q}$ will be less prevalent than those at $\phi^{\vec{n}}_{p:q}$ for small domain sizes, and the total lengths of $\phi^{\vec{n}}_{p:q}$ and $\phi^{\vec{l}}_{p:q}$ interfaces will become increasingly similar as domain sizes increase.

To complete our calculation of the equilibrium T′60T′ domain shapes in $MoTe_2$, we minimize the total energy

TABLE I. Components of the T′ → T′ transformation strain tensors $\epsilon^0_{ij}(p{:}q)$ and related quantities for transformations between T′ orientational variant pairs in {Mo,W}{S,Se,Te}$_2$. Upon rotation by $\psi_{p:q}$, each $p{:}q$ pair generates the same set of measures deriving from the diagonalized matrix $\tilde{\epsilon}^0_{ij} = [\tilde{\epsilon}^0_{xx}, \tilde{\epsilon}^0_{yy}] = \tilde{\epsilon}^0_s[(\tilde{R}+1), (\tilde{R}-1)]$, which has shear component $\tilde{\epsilon}^0_s = (\tilde{\epsilon}^0_{xx} - \tilde{\epsilon}^0_{yy})/2$ and dilatation ratio $\tilde{R} = (\tilde{\epsilon}^0_{xx} + \tilde{\epsilon}^0_{yy})/(\tilde{\epsilon}^0_{xx} - \tilde{\epsilon}^0_{yy})$. The fractional area change is $\tilde{\Delta}A/A = \tilde{\epsilon}^0_{xx} + \tilde{\epsilon}^0_{yy} + \tilde{\epsilon}^0_{xx}\tilde{\epsilon}^0_{yy}$. T′ lattice constants are from Ref. [8].

	$\psi_{1:2}$	$\psi_{1:3}$	$\psi_{2:3}$	$\tilde{\epsilon}^0_{xx}$	$\tilde{\epsilon}^0_{yy}$	$\tilde{\epsilon}^0_s$	$\tilde{R}$	$\tilde{\Delta}A/A$
MoS_2	105.23°	−14.77°	225.23°	0.0355	−0.0335	0.0345	0.0290	0.0012
$MoSe_2$	104.87°	−15.13°	224.87°	0.0437	−0.0397	0.0417	0.0480	0.0017
$MoTe_2$	104.69°	−15.31°	224.69°	0.0609	−0.0529	0.0569	0.0703	0.0033
WS_2	104.52°	−15.48°	224.52°	0.0302	−0.0282	0.0292	0.0343	0.0009
WSe_2	105.02°	−14.98°	225.02°	0.0355	−0.0325	0.0340	0.0441	0.0012
WTe_2	104.65°	−15.35°	224.65°	0.0392	−0.0352	0.0372	0.0537	0.0014

including both the elastic misfit (based on the transformation strains in Table I) and anisotropic interface energy contributions. For the elastic contributions, we apply the Eshelby approach to evaluate the elastic energy of a coherent misfitting elliptical inclusion in an infinite matrix in 2D. The matrix and inclusion are taken to have the same (isotropic) elastic moduli and plane stress conditions are applied. For arbitrary ellipse inclination ζ, area $A_0 = \pi R_1 R_2$, and misfit strain tensor ϵ^0_{ij}, the elastic energy is given by $E^{\text{elas}} = E_0(\zeta, A_R, \epsilon^0_{ij})R_1R_2$, where $E_0(\zeta, A_R, \epsilon^0_{ij})$ is defined in Eq. (D5). R_1 and R_2 are the semimajor and semiminor radii, respectively, of the ellipse. This equation, with $\zeta = \phi^{\vec{n}}_{p:q}$ from Table II and $\epsilon^0_{ij} = \tilde{\epsilon}^0_{ij}$ from Table I, are assumed to provide a reasonable approximation of the elastic energy of the nearly rectangular T′ domains. The effect of interfacial anisotropy is incorporated by assuming that the interfacial energy of the embedded domain is always given by that of a rectangle in the preferred orientation $\zeta = \phi^{\vec{n}}_{p:q}$ from Table II and Fig. 3(b). The total interfacial energy is then approximated as $E^{\text{int}} \simeq 2\sqrt{\pi}[\gamma_{1:2}(-30°)R_1 + \gamma_{1:2}(60°)R_2]$.

For a domain size $L_0 = 2\sqrt{R_1R_2}$, the total energy $E^{\text{elas}} + E^{\text{int}}$ is numerically minimized with respect to $A_R = R_1/R_2$. $A_R(L_0)$ is shown in Fig. 3(c). It correctly converges to the zero-misfit limit as $L_0 \to 0$, i.e., $A_R \simeq 2.27$ [see Fig. 3(b)]. With increasing L_0, the bulk elastic energy becomes more significant. Though elastic and interfacial contributions favor nearly the same interface inclinations, the elastic energy is minimized at increasingly large A_R. The nearly rectangular shape and preferred orientation are therefore maintained as an isolated domain grows, but the axial ratio of the rectangle increases dramatically from $A_R \simeq 4$ to 100 as L_0 increases from 10 nm to 2 μm. The origin of the scaling relation $A_R \sim L_0^{2/3}$ seen in Fig. 3(c) at large L_0 is described in the following subsection.

Isolated domains of T′ variant q embedded within large domains of variant $p \neq q$ are most likely to appear within a T′ monolayer that has been prestrained to create an initial state with only one or two variant orientations. A change in applied strain state can lead to the formation of the one or two orientations not initially present, and these newly formed q domains will be embedded within the preformed $p \neq q$ microstructure.

This scenario is less probable when the initial state contains all three T′ orientations; three-variant domain morphologies are qualitatively different from those with only one or two variants. Global strain-accommodating morphologies in such cases contain nested threefold star patterns, radial 30° wedge/fan patterns, and fourfold domain wall junctions, as shown in Ref. [10]. When the applied strain state is changed in a T′ monolayer containing pre-existing microstructures with these symmetries, the pre-existing T′/T′ interfaces can simply propagate in the direction of the disfavored variants, expanding the size of the favored variants without requiring nucleation of embedded domains. Though the evolving domain shapes will be determined more by the initial three-variant microstructure than by spontaneous formation of new embedded domains, the habit inclinations listed in Table II will nonetheless dominate the microstructure at all stages and T′/T′ interface coherency should be maintained.

TABLE II. Inclinations of minimum T′60T′ interfacial energy, $\phi^{\text{int}}_{p:q}$, and elastic energy minimizing T′60T′ interface inclinations (habits), $\phi^{\vec{n}}_{p:q}$ and $\phi^{\vec{l}}_{p:q}$, for all group VI TMD monolayers and all orientational variant pairs. Interfacial energies are determined from DFT calculations, and habit inclinations are determined from continuum elasticity via the interface normal vectors $\vec{n} = [\sqrt{\tilde{\epsilon}^0_{xx}/(\tilde{\epsilon}^0_{xx} - \tilde{\epsilon}^0_{yy})}, \sqrt{-\tilde{\epsilon}^0_{yy}/(\tilde{\epsilon}^0_{xx} - \tilde{\epsilon}^0_{yy})}]$ and $\vec{l} = [\sqrt{\tilde{\epsilon}^0_{xx}(\tilde{\epsilon}^0_{xx} - \tilde{\epsilon}^0_{yy})}, -\sqrt{-\tilde{\epsilon}^0_{yy}(\tilde{\epsilon}^0_{xx} - \tilde{\epsilon}^0_{yy})}]$. T′ lattice constants are from Ref. [8].

	$\phi^{\text{int}}_{1:2}$	$\phi^{\vec{n}}_{1:2}$	$\phi^{\vec{l}}_{1:2}$	$\phi^{\text{int}}_{1:3}$	$\phi^{\vec{n}}_{1:3}$	$\phi^{\vec{l}}_{1:3}$	$\phi^{\text{int}}_{2:3}$	$\phi^{\vec{n}}_{2:3}$	$\phi^{\vec{l}}_{2:3}$
MoS_2	60°	59.4°	−28.9°	−60°	−60.6°	31.1°	0°	−0.6°	91.1°
$MoSe_2$	60°	58.5°	−28.8°	−60°	−61.5°	31.2°	0°	−1.5°	91.2°
$MoTe_2$	60°	57.7°	−28.3°	−60°	−62.3°	31.7°	0°	−2.3°	91.7°
WS_2	60°	58.5°	−29.5°	−60°	−61.5°	30.5°	0°	−1.5°	90.5°
WSe_2	60°	58.8°	−28.7°	−60°	−61.2°	31.3°	0°	−1.2°	91.3°
WTe_2	60°	58.1°	−28.8°	−60°	−61.9°	31.2°	0°	−1.9°	91.2°

TABLE III. Inclinations of minimum H0T′ interfacial energy, $\phi^{\rm int}_{\rm H0T'}$ (assumed), and elastic energy minimizing H0T′ interface inclinations (habits), $\phi^{\vec{n}}_p$ and $\phi^{\vec{l}}_p$, for all group {Mo,W}{S,Se,Te}$_2$ monolayers and orientation variants. Interfacial energies are determined from DFT calculations, and habit inclinations are determined from continuum elasticity as described in Table II. T′ lattice constants are from Ref. [8].

	$\phi^{\rm int}_{\rm H0T'}$	$\phi^{\vec{n}}_1$	$\phi^{\vec{l}}_1$	$\phi^{\rm int}_{\rm H0T'}$	$\phi^{\vec{n}}_2$	$\phi^{\vec{l}}_2$	$\phi^{\rm int}_{\rm H0T'}$	$\phi^{\vec{n}}_3$	$\phi^{\vec{l}}_3$
MoS_2	0°	10.34°	−10.34°	−60°	−49.66°	−70.34°	60°	70.34°	49.66°
$MoSe_2$		28.46°	−28.46°		−31.54°	−88.46°		88.46°	31.54°
$MoTe_2$	0°	41.78°	−41.78°	−60°	−18.22°	78.22°	60°	−78.22°	18.22°
WS_2		(∼0°)			(∼−60°)			(∼60°)	
WSe_2		19.82°	−19.82°		−40.18°	−79.82°		79.82°	40.28°
WTe_2		38.59°	−38.59°		−21.41°	81.41°		−81.41°	21.41°

C. H0T′ interfaces and domains

1. Flat 2D monolayers

In this subsection, we consider the case of flat TMD monolayers, e.g., monolayers bonded to substrates. A large number of distinct, coherent heterophase interfaces can occur between H and T′ domains, as recently studied for MoS_2 via first-principles methods [28]. Analysis of $MoTe_2$ H0T′ interfaces and the morphologies of embedded T′ domains following the above approach for T′60T′ would require DFT relaxation calculations for a minimum of 60 different configurations (interface pairs), each at two or more values of Te chemical potential $\mu_{\rm Te}$. To simplify this undertaking, we make a series of approximations and estimate the expected range of deviation from our predictions.

The computed habit inclinations of H0T′ interfaces are shown in Table III, and interfacial energies in $MoTe_2$ at $\phi = 0°$ and $\phi = 41.78°$ (near the H0T′ $p = 1$ habit inclination at $\phi^{\vec{n}}_1 = 40.89°$) computed from first principles [10] are shown in Fig. 4(a). Like T′60T′ domains, both interfacial and elastic misfit energies contribute to H0T′ morphologies. Unlike T′60T′ domains, the interfacial and elastic misfit energies of H0T′ domains do not favor the same interface inclinations. The energy of the $\phi = 0°$ interface pair is significantly lower than that of the near-habit pair. The morphology of isolated T′ domains during an H → T′ transformation will therefore vary with domain size and will be determined by the competition between quasi-1D interfacial and quasi-2D bulk elastic effects. Interfacial effects will dominate at small domain sizes, favoring compact domains, and elastic misfit effects will dominate at large domain sizes, favoring needlelike domains; the crossover occurs at L^*_0.

We assume a functional form for $\gamma^{\rm H0T'}(\hat{\phi})$ based on the approximation that the threefold and dual twofold symmetries of the H and T′ lattices, respectively, combine additively to determine the symmetry of $\gamma^{\rm H0T'}(\hat{\phi})$:

$$\gamma^{\rm H0T'}(\hat{\phi}) = \frac{\bar{\gamma}_{\rm H0T'}}{2}\{2 + \epsilon_{\rm H0T'}[\cos(4\hat{\phi} - \pi) + \cos(6\hat{\phi})]\}, \tag{19}$$

where $\bar{\gamma}_{\rm H0T'}$ and $\epsilon_{\rm H0T'}$ are free constants. The best fit to this functional form and the resulting Wulff construction (in the absence of misfit strain) are shown in Figs. 4(a) and 4(c). Using these approximations, the equilibrium shape of a T′ domain embedded within an infinite H monolayer in the absence of misfit strain (i.e., very small domain sizes) is nearly hexagonal. The orientation of the hexagon for each variant is shown for completeness. Each is slightly elongated along the a axis of the T′ lattice because $\gamma^{\rm H0T'}(0°) > \gamma^{\rm H0T'}(90°)$ [see Eq. (19)].

Our DFT calculations (and symmetry considerations) demonstrate that the energies of interfaces on opposite sides of a T′ domain created by a single shuffle operation are generally unequal. This is because one interface is Te- or Te/Mo-rich while the other is Te- or Te/Mo-poor. These interfacial energies and their differences therefore depend on $\mu_{\rm Te}$. The domain morphologies that result when opposing interfaces have unequal energy are qualitatively similar to those on the right side of Fig. 4(c). In general, though the number of sides and the details of the domain symmetry depend on the full form of $\gamma^{\rm H0T'}(\hat{\phi})$ for a given $\mu_{\rm Te}$, single T′ variant domains with $L_0 \ll L^*_0$ remain relatively compact with preferred inclinations at multiples of 30°, 60°, or 90°. The computed difference between $\gamma^{\rm H0T'}(90°)$ and $\gamma^{\rm H0T'}(58.22°)$ further suggests that the domains are likely faceted.

Next, we consider the effect of misfit strain (as in the previous section), but instead of minimizing the total energy with respect to the shape of a single domain, we minimize with respect to two domains; a compact shape such as those shown in Fig. 4(c) and an elongated shape that is free to rotate. The shape with lowest total energy at a given L_0 corresponds to the equilibrium shape, and a crossover from compact to elongated morphologies occurs above domain size L^*_0.

The calculation described above requires solving $E^{\rm tot}_{\rm com} - E^{\rm tot}_{\rm elo} = \Delta E^{\rm tot} = 0$ for L_0, where $E^{\rm tot}_{\rm com}$ and $E^{\rm tot}_{\rm elo}$ are the total interfacial plus elastic misfit energies of the optimized compact and elongated domains, respectively, at a given L_0. The general solution of this equation (see Appendix D) is

$$L^*_0 = \frac{4(\bar{P}_{\rm elo}\bar{\gamma}_{\rm elo} - \bar{P}_{\rm com}\bar{\gamma}_{\rm com})}{E_0\left(\zeta = 0, A_R = 1, \epsilon^0_{ij}\right) - E_0\left(\zeta, A_R, \epsilon^0_{ij}\right)}, \tag{20}$$

where $\bar{P}_{\rm elo}$ and $\bar{P}_{\rm com}$ are the two domain perimeter lengths scaled relative to L_0, $\bar{\gamma}_{\rm elo}$ and $\bar{\gamma}_{\rm com}$ are the mean interfacial energies, and $E_0(\zeta = 0, A_R = 1, \epsilon^0_{ij})$, $E_0(\zeta, A_R, \epsilon^0_{ij})$ are the elastic energy prefactors defined in Eq. (D5) for the optimized compact and elongated domains, respectively. The form of this result shows that L^*_0 is controlled by the ratio of the differences between the average interfacial energy densities and the total elastic energy densities of the two domain shapes.

To prescribe a particular solution for isolated T′ domains in H-TMD monolayers, we approximate the elastic energy of the compact domain as that of a circle with diameter L_0; $E^{\rm elas}_{\rm com} = E_0(\zeta = 0, A_R = 1, \epsilon^0_{ij})L_0^2/4$. The elastic energy

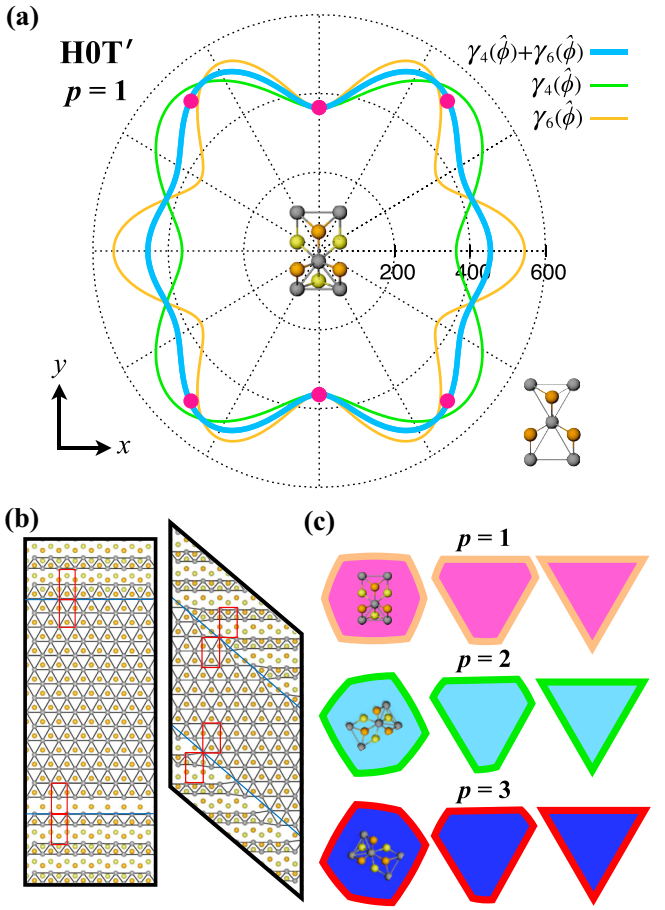

FIG. 4. H0T′ interfacial energy and interfacially-preferred T′ domain shapes. (a) H0T′($p = 1$) interfacial energy $\gamma^{\mathrm{H0T'}}(\hat{\phi})$. Energy units are meV/Å. Data points correspond to DFT results from the simulation configurations shown in (b), thin solid lines are expressions with four- and sixfold symmetry ($\gamma_n(\hat{\phi}) = \bar{\gamma}[1 + \epsilon\cos(n\hat{\phi})]$), and the thick solid line is the best fit to Eq. (19). (b) Top views of the relaxed H0T′ interfaces at $\phi = 0°$ and $\phi = 40.89°$ from DFT. Blue and black lines denote interfaces and 'bonds' between nearest neighbor Mo atoms, respectively, and red rectangles highlight H and T′ unit cells. (c) Left: Equilibrium zero-misfit domain shapes for each T′ variant orientation p [from the Wulff construction employing the blue line in (a)]. Center, right: A similar $\gamma^{\mathrm{H0T'}}(\hat{\phi})$ that assumes asymmetry in the energies of opposing interfaces across the domain, for intermediate and high asymmetries. Neglecting misfit strain implies that these shapes are valid only for $L_0 \ll L_0^*$.

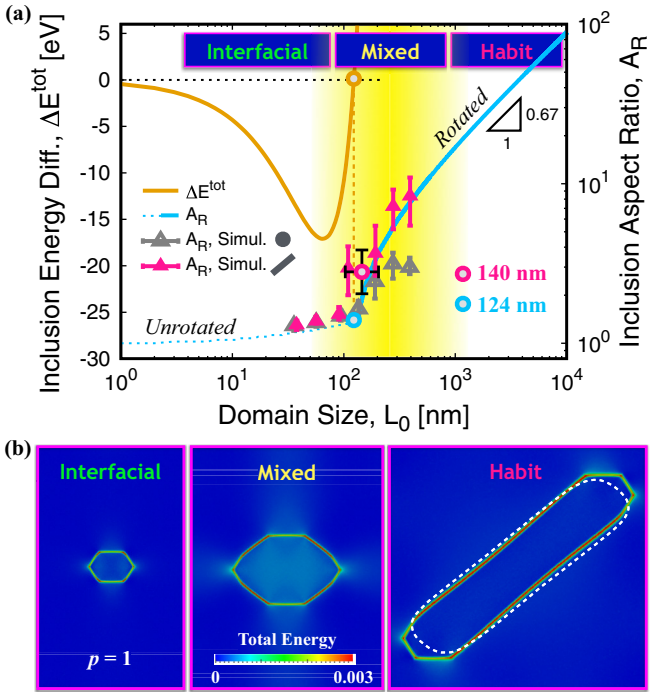

FIG. 5. Morphologies of single T′ domains in flat H-$MoTe_2$ sheets. (a) Inclusion energy difference ΔE^{tot} and domain aspect ratios A_R vs domain size L_0, determined via the modified Eshelby approach described in the text for one value of Te chemical potential μ_{Te}. Crossover from compact interface-dominated domains to elongated misfit-dominated (habit) domains occurs at the L_0^* values marked with closed circles. Values obtained analytically and from simulations are in good agreement. Initial domain shapes in simulations are indicated in the legend. The shaded yellow area approximates the intermediate coexistencelike regime in which metastable domains of mixed morphology also appear. (b) Maps of combined interfacial and elastic energy for stable embedded T′ domains of various size. The white dashed line in the rightmost panel outlines the domain shape obtained without interfacial anisotropy.

of the elongated and rotated domain is approximated for an ellipse with inclination ζ and area $A_0 = \pi L_0^2/4 = \pi R_1 R_2$: $E_{\mathrm{elo}}^{\mathrm{elas}} = E_0(\zeta, A_R, \epsilon_{ij}^0) R_1 R_2$.

For the interfacial contribution, $E_{\mathrm{com}}^{\mathrm{int}}$, the relevant energies given by the best fit to Eq. (19) are summed over the six sides of the perimeter P_{hex} of the hexagon. For $E_{\mathrm{elo}}^{\mathrm{int}}$, we assume an elliptical domain shape with arbitrary inclination ζ and aspect ratio $A_R = R_1/R_2$. The interfacial energy can then be expressed as a modulated elliptic integral,

$$E_{\mathrm{elo}}^{\mathrm{int}} = 2R_1 \int_0^{\pi} d\zeta' \gamma^{\mathrm{H0T'}}(\tau - \zeta')\sqrt{1 - e^2 \sin^2 \zeta'}, \qquad (21)$$

where ζ' is the polar angle from the ellipse center, $e = \sqrt{1 - R_2^2/R_1^2}$ is the eccentricity, and $\tau(\zeta', e) = \arctan[\tan \zeta'/(1 - e^2)]$ is the angle normal to the ellipse perimeter at ζ'. Additional details are in Appendix D.

To obtain a complete solution, L_0^* [Eq. (20)] must be minimized with respect to ζ and A_R as a function of L_0. Results for $MoTe_2$, displayed in Fig. 5(a), show that the minimized $\Delta E^{\mathrm{tot}} = 0$ at $L_0^* \simeq 124$ nm. For $L_0 < L_0^*$, A_R increases weakly above 1 nm as the balance of interfacial and elastic energies favors a compact shape with only slight elongation. Here $E_{\mathrm{elo}}^{\mathrm{tot}} > E_{\mathrm{com}}^{\mathrm{tot}}$, and the hexagon is preferred. At or near L_0^*, a kink in A_R appears. Here, when elongated domains become preferred, the ζ that minimizes the energy quickly rises to ϕ_{habit} and A_R increases more rapidly with L_0. This analysis indicates that a compact T′ domain of size $L_0 \ll L_0^*$ will initially grow with nearly fixed shape until $L_0 \simeq L_0^*$, elongating slightly (along the a axis of the T′ unit cell) as $L_0 \to L_0^*$. For $L_0 \gtrsim L_0^*$, if barriers to shape change are low, the domain will rapidly rotate its weakly elongated axis to align with ϕ_{habit} and then begin to elongate at a much greater

rate. This elongation at fixed ζ will continue indefinitely with a sublinear scaling, $A_R \sim L_0^s$, where $s \simeq 2/3$.

The power law exponent $s = 2/3$ seen at large L_0 can be derived as follows. The aspect ratio is determined by the competition between interfacial and bulk elastic energies. For $A_R \gg 1$, $E_{\rm elo}^{\rm int}$ is approximately that of a rectangular domain,

$$E_{\rm elo}^{\rm int} \approx 2\bar{\gamma}_{\rm H0T'}(R_1 + R_2) = \bar{\gamma}_{\rm H0T'} L_0 (A_R + 1)/\sqrt{A_R} \approx \bar{\gamma}_{\rm H0T'} L_0 \sqrt{A_R} \quad (22)$$

to leading order in A_R. At $\zeta = \phi_{\rm habit}$ and $A_R \gg 1$, Eq. (D5) shows that $E_{\rm elo}^{\rm elas} \sim L_0^2(1 + A_R^{-1})$ (to leading order in A_R). Minimizing $E_{\rm elo}^{\rm elas} + E_{\rm elo}^{\rm int}$ with respect to A_R gives

$$A_R \approx (E_A L_0)^{2/3}, \quad (23)$$

which agrees well with the numerically-determined s values shown in Figs. 3(c), 5(a), and 11(c). The prefactor

$$E_A = \frac{\pi\mu(1+\nu)h\left[3\epsilon_{xx}^0\epsilon_{xx}^0 - 2\epsilon_{xx}^0\epsilon_{yy}^0 - \epsilon_{yy}^0\epsilon_{yy}^0 - 4\epsilon_{xy}^0\epsilon_{xy}^0\right]}{2\bar{\gamma}_{\rm H0T'}} \quad (24)$$

is the ratio of elastic to interfacial energies, which directly reflects the underlying physics.

Our continuum simulations, parameterized for $MoTe_2$ with the anisotropic interfacial energy of Fig. 4(a) and Eq. (19), corroborate these calculations (see Fig. 5). The large interfacial anisotropy and domain faceting is accommodated in these simulations by convexifying the interface energy [51]. Simulations were conducted by seeding an H monolayer with a single $p = 1$ T′ domain and allowing it to relax at fixed T′ area (see Appendix B). Systems initialized with small ($L_0 \lesssim 100$ nm) T′ domains (either circular or rectangular with $A_R = 2$–15 and $\zeta = \phi_{\rm habit}$) relax to compact faceted shapes determined by the anisotropic interfacial energy [Fig. 5(b) left]. Systems initialized with large ($L_0 \gtrsim 100$ nm) circular T′ domains tend to remain compact, but an increasing fraction of the perimeter becomes habit aligned in a metastable coexistencelike configuration of mixed character [Fig. 5(b) center]. Systems initialized with large ($L_0 \gtrsim 100$ nm) rectangular, habit-aligned T′ domains relax to increasingly elongated, habit-aligned shapes with increasing L_0 [Fig. 5(b) right]. The total energy of the elongated domains becomes lower than that of the compact domains for 100 nm $\lesssim L_0^* \lesssim$ 200 nm, in good agreement with the analytic results ($L_0^* \simeq 124$ nm).

The agreement between L_0^* values obtained using the above two approaches demonstrates the efficacy of the semianalytic Eshelby-type analysis, although both approaches employ input parameters that are somewhat uncertain and include simplifying assumptions. It is therefore prudent to estimate the overall uncertainty associated with these results. According to Eq. (20), L_0^* varies with the monolayer elastic constants as $L_0^* \sim [\mu(1+\nu)h]^{-1}$ and with average H0T′ interfacial energies as $L_0^* \sim \bar{\gamma}_{\rm elo} - \bar{\gamma}_{\rm com}$ (assuming that $\bar{P}_{\rm elo} \simeq \bar{P}_{\rm com}$ or $A_R \sim 1$ at L_0^*). Conservatively employing uncertainties of $\mu \simeq 50 \pm 20$ GPa, $\nu \simeq 0.24 \pm 0.06$, $h \simeq 0.5 \pm 0.15$ nm, and $\bar{\gamma}_{\rm elo} - \bar{\gamma}_{\rm com} \simeq \gamma^{\rm H0T'}(\hat{\phi}_{\rm habit}) - \gamma^{\rm H0T'}(90^\circ) \simeq 146 \pm 100$ meV/Å, we obtain 27 nm $\lesssim L_0^* \lesssim$ 680 nm.

The case of a single, isolated T′ variant domain is most relevant to transformations biased by strain or other external controls such that formation of a single variant orientation is preferred. This case is less relevant if two or three variant orientations can easily form and combine into composite domain structures (wedges, fans, threefold stars, etc.) that accommodate the misfit strain more effectively than single variant domains. Such composite T′ structures will also be subject to a competition between interfacial and misfit strain energies, but a full morphological analysis requires knowledge of their elastic energy minimizing shapes. The elastic energies of some likely composite structures such as wedges can be determined analytically. A complementary approach is to allow our PFM simulations to solve the problem stochastically. The most prevalent structures, composite or univariant, that spontaneously nucleate and grow can be identified as the configurations that best accommodate the elastic misfit energy.

2. *Bendable 2D monolayers*

In TMD monolayers that are free to deform out-of-plane (sheets not bonded to substrates), a large portion of the in-plane misfit strain associated with an isolated T′ domain may be relieved through localized buckling at very low bending energy cost. Domains in bendable sheets will therefore retain compact, interfacial energy-dominated shapes to larger sizes than in constrained flat sheets. However, a quantitative analysis of domain shapes in bendable monolayers presents significant challenges. The primary difficulty stems from the elastic coupling between the T′ domain and the surrounding H matrix, which leads to nontrivial buckling morphologies and strain states. Buckling induced by an elastically misfitting T′ domain is spatially heterogeneous and may occur locally in either (both) phase(s) wherever the strain is sufficiently compressive.

A $p = 1$ T′ domain, for example, tends to buckle internally along b, the direction of maximum compressive misfit, with the buckle amplitude decreasing to zero some distance into the adjacent H phase. Tensile strain is therefore induced within the H phase near T′ domain ripples, and this strain increases with ripple amplitude and wavelength. The surrounding H matrix also tends to buckle near H/T′ interfaces with ϕ near zero but with buckling along a, the direction of maximum compression induced by the adjacent T′ domain. The nontrivial buckle morphology and strain state of the energy minimizing domain shape is dictated by the competition between misfit strain relieved via buckling and strain concurrently induced in the nearby H phase.

We therefore utilize continuum PFM simulations to examine the morphologies of isolated T′ domains in bendable monolayers; results are shown in Fig. 6. Domains with $L_0 \lesssim$ 50 nm remain hexagonal with $A_R \approx 1$, slightly more compact than in flat monolayers at equivalent sizes. Small amplitude out-of-plane deformations do occur within and around the domain but it is best characterized as slightly folded rather than buckled or rippled. For 50 nm $\lesssim L_0 \lesssim$ 400 nm, the hexagons become rippled (more than one buckling period) and slightly elongated along b ($A_R < 1$). For 400 nm $\lesssim L_0 \lesssim$ 2 μm, the domains remain rippled but become increasingly elongated along a as L_0 increases ($A_R > 1$). Due to computational limitations we were unable to observe a crossover to

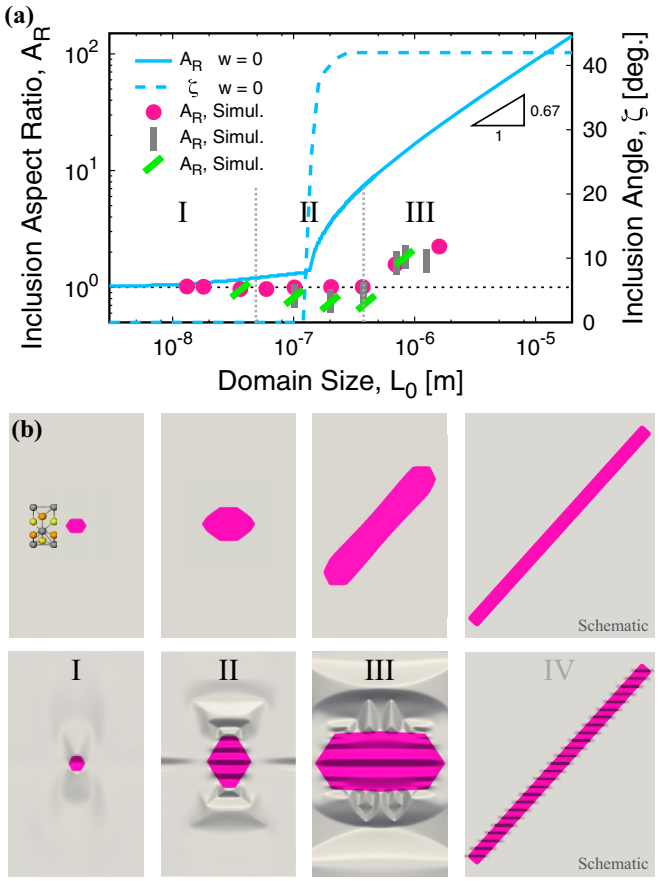

FIG. 6. Morphologies of single T′ domains in bendable H-$MoTe_2$ sheets. (a) Inclusion aspect ratios A_R and inclination angle ζ vs domain size L_0. Crossover from compact semiflat to compact buckled occurs near $L_0 = 50$ nm, from compact buckled to a-elongated buckled near $L_0 = 400$ nm, and from a-elongated buckled to habit elongated buckled above $L_0 = 2\ \mu$m. Symbols denote simulations initialized with different domain shapes; circles ≡ compact, vertical rectangles ≡ b elongated, and tilted rectangles ≡ habit-aligned elongated. Solid lines are analytic results for flat monolayers. (b) Equilibrium $p = 1$ domain shapes determined from continuum simulations without bending (upper) and with bending (lower) in the regimes highlighted in (a). $w(\vec{r})$ is amplified by a factor of five to enhance visual contrast. Regimes I/II and III/IV are not qualitatively different for flat monolayers. Schematics are shown for the largest domain size, which is not computationally accessible.

habit-aligned needlelike shapes, but the results indicate that L_0^* for this crossover is at least an order of magnitude larger than that in flat monolayers.

These results can be understood qualitatively as follows. The small domains of regime I [see Fig. 6(a)] induce small amplitude bending (magnitude $\lesssim 1$Å) and do not ripple internally with more than half of a buckling period because the bending energy of true rippling would exceed the in-plane misfit strain energy relieved. Misfit strain energy scales as $\sigma_{ij}^0 \epsilon_{kl}^0 L_0^2$, while bending energy scales as $\kappa(\nabla^2 w)^2 L_0^2$ or as $\kappa A^2 L_0^2/\lambda^4$ if $w = A\sin(2\pi x/\lambda)$. For $\lambda \approx L_0$ and A constant (valid for small λ), bending energy scales as $1/L_0^2$ and buckling is suppressed below a threshold L_0 value.

In regime II, the T′ domains are large enough to ripple internally and relieve a significant portion of the in-plane misfit strain at increasingly small bending energy cost. Unlike flat monolayers at equivalent domain sizes, elastic energy remains comparable to interfacial energy in this regime and the domains remain compact and faceted well above the L_0^* of flat monolayers.

Total elastic energy eventually exceeds total interfacial energy at the beginning of regime III. However, rather than inducing a crossover to habit-aligned needlelike domains as in flat monolayers, a crossover to relatively weakly a-elongated domains is induced. This is because buckling relieves much of the bulk misfit strain energy, and the total energetic cost of bending is extremely small due to the minuscule bending stiffness of 2D materials. The dominant portion of the elastic energy in buckled compact domains comes instead from residual in-plane strain in the vicinity of each H/T′ interface that cannot be fully accommodated by buckling. The energies of the two domain shapes can thus be decomposed as

$$E_{\rm com}^{\rm tot} = E_{\rm com}^{\rm int} + E_{\rm com}^{\rm bend} + E_{\rm com}^{\rm res} \tag{25}$$

$$E_{\rm elo}^{\rm tot} = E_{\rm elo}^{\rm int} + E_{\rm elo}^{\rm bulk}, \tag{26}$$

where superscripts 'bend' and 'res' denote bending and residual in-plane misfit energy. Since $E_{\rm com}^{\rm int} < E_{\rm elo}^{\rm int}$, compact shapes remain the lower energy structures until their total bending plus residual misfit strain energy becomes large enough to cancel this interfacial advantage.

In regime III, where $E_{\rm com}^{\rm bend} \ll E_{\rm com}^{\rm res}$, domain shape is primarily controlled by the competition between interfacial energy, which prefers a hexagonal shape, and residual misfit energy, which also prefers a relatively compact shape (minimal perimeter length) albeit not a perfect hexagon. This is evidenced by the fact that domains in regime III elongate along a, as shown in Fig. 6. Interfaces with inclination $\phi \approx 0^\circ$ carry less misfit strain ($\epsilon_{xx}^0 = -0.0299$) than those with $\phi \approx 90^\circ$ ($\epsilon_{yy}^0 = 0.0374$), so the proportion of $\phi \approx 0^\circ$ interface length increases to minimize the total residual misfit energy. Otherwise identical simulations conducted with ϵ_{yy}^0 reduced from 0.0374 to 0.01 further support this analysis. Such domains instead elongate along b in regime III to minimize the larger residual misfit energy along a.

To examine the competition between compact and elongated shapes more closely, we first ask whether a crossover to habit-aligned needlelike shapes must occur. This question can be answered by determining the L_0 dependencies of each term in Eqs. (25) and (26), that with the weakest divergence as $L_0 \to \infty$ is preferred at large domain sizes. For compact domains $E_{\rm com}^{\rm int} \sim L_0$, and we expect $E_{\rm com}^{\rm res}$ to be proportional to the total interfacial length P times the buckle wavelength λ (a type of Saint-Venant's principle). We postulate that $\lambda \sim L_0^\delta$, where the exponent $0 \leqslant \delta \leqslant 1$ is determined by the nonlinear interplay between bending strains and in-plane strains. This gives $E_{\rm com}^{\rm res} \sim L_0^{1+\delta}$. As discussed above, bending energy scales as $\kappa A^2 L_0^2/\lambda^4$ for sinusoid-type morphologies, $w = A\sin(2\pi x/\lambda)$. Note that even though the bending energy is a bulk 2D quantity, it does not in general scale as L_0^2 due to its dependence on A and λ, which also generally vary with L_0. The above postulate that $\lambda \sim L_0^\delta$ gives $E_{0,\rm com}^{\rm bend} \sim L_0^{2(1-\delta)}$.

For elongated domains $P \sim L_0(A_R+1)/\sqrt{A_R}$, and we have further shown above that $A_R \sim L_0^s$ for large A_R, with $s \approx 2/3$. This gives $E_{\rm elo}^{\rm int} \sim L_0^{1+s/2} = L_0^{4/3}$ for elongating domains with large A_R. The form of $E_{\rm elo}^{\rm bulk}$ follows from Eq. (D5) as $L_0^{2-s} = L_0^{4/3}$ for large A_R. Gathering terms, Eqs. (25) and (26) become

$$E_{\rm com}^{\rm tot} = E_{0,\rm com}^{\rm int} L_0 + E_{0,\rm com}^{\rm bend} L_0^{2(1-\delta)} + E_{0,\rm com}^{\rm res} L_0^{1+\delta} \quad (27)$$

$$E_{\rm elo}^{\rm tot} = \left(E_{0,\rm elo}^{\rm int} + E_{0,\rm elo}^{\rm bulk}\right) L_0^{4/3}, \quad (28)$$

where $E_{0,i}^{j}$ are prefactors for interfacial, residual, bending, and bulk energy.

In the regime of large L_0 the dominant term for compact domains is $E_{0,\rm com}^{\rm bend} L_0^{2(1-\delta)}$ for $\delta < 1/3$ and $E_{0,\rm com}^{\rm res} L_0^{1+\delta}$ for $\delta > 1/3$. For $\delta = 1/3$, the energies of both compact and elongated domains scale as $L_0^{4/3}$ and the existence of a crossover is not guaranteed; this will depend on the values of the energy prefactors. For $\delta \neq 1/3$, the energy of compact domains scales faster than $L_0^{4/3}$, implying that, asymptotically, elongated domains must become the equilibrium shape. For $\delta < 1/3$ bending energy eventually dominates, while for $\delta > 1/3$ residual misfit strain energy eventually dominates. The former corresponds to buckle wavelength varying weakly with domain size and residual misfit energy therefore behaving as a quasi-1D effect. The latter corresponds to buckle wavelength varying more dramatically with domain size and residual misfit energy therefore behaving as a quasi-2D effect. For either case, we can conclude that sufficiently large domains will prefer habit-aligned needlelike shapes in bendable monolayers.

The domain size L_0^* at which this crossover occurs will depend sensitively on the energy prefactors and the scaling exponents δ and s. A reliable estimation of its value is therefore not provided here; a fully quantitative analysis or larger-scale numerical simulations are needed.

If the monolayer is on a substrate, the domain size L_0^* at which any shape crossover occurs will vary with the monolayer-substrate interaction strength. Systems with very weak interactions will exhibit the type of behavior shown in Fig. 6(a), while the size at which crossover to habit-aligned needlelike domains occurs will decrease as interaction strength increases, ultimately approaching the behavior shown in Fig. 5(a) for flat monolayers. This interaction can therefore be employed to tunably control L_0^* and T′ domain geometry in partially-transformed monolayers.

IV. MECHANICAL RESPONSE

A preliminary account of the stress-strain response of $MoTe_2$ monolayers undergoing a H → T′ transformation was reported in Ref. [10]. The effective elastic moduli of such monolayers (through the range of strains corresponding to H/T′ coexistence) were shown to vary widely with applied strain. An effective modulus of zero (i.e., a superelastic response) was found to occur at $\bar{\epsilon}_{ij} = \epsilon_{ij}^0(p)$ for any single variant p. Here we expand on these results and present new findings for bendable T′ WTe_2 monolayers, which have been predicted to be ferroelastic and possibly shape memory materials [8].

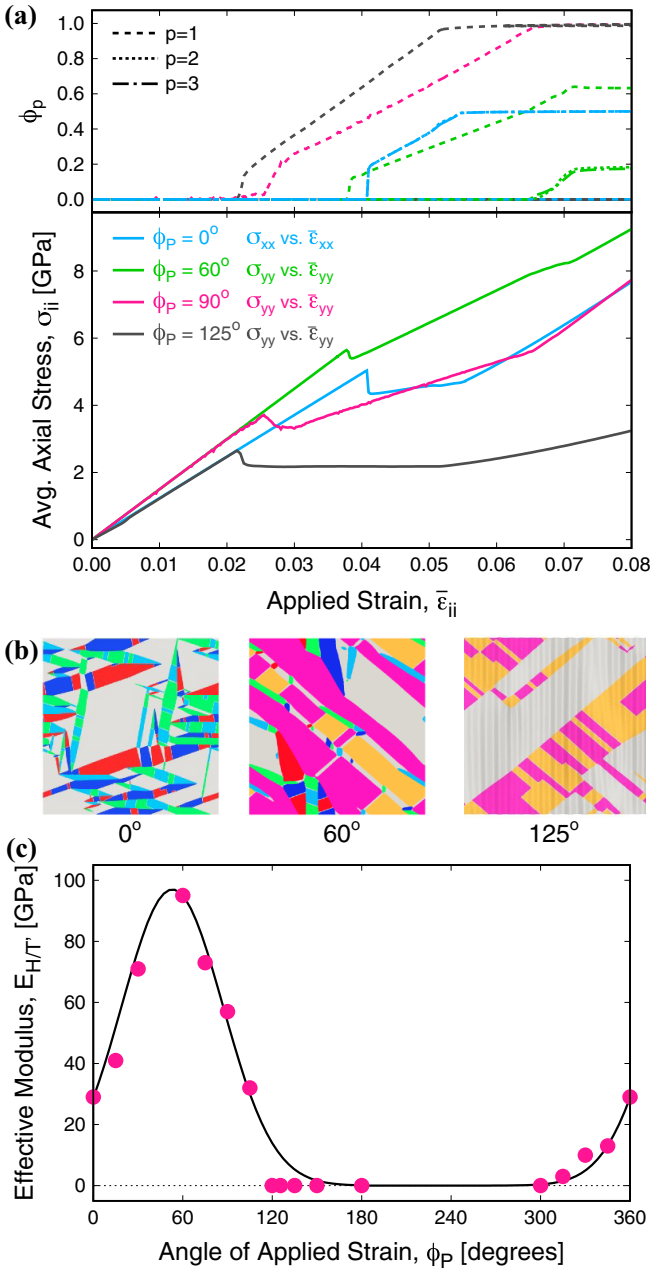

FIG. 7. Mechanical response of transformable, freely suspended $MoTe_2$ monolayers. (a) Stress-strain curves obtained for various applied strains (lower) and the corresponding variations in area fraction of T′ variants (upper). (b) Representative domain configurations for $\phi_P = 0°$, 60°, and 125°. (c) Variation of the effective H/T′ coexistence elastic modulus with $\phi_P = \arctan(\bar{\epsilon}_{yy}/\bar{\epsilon}_{xx})$ at $\phi_L = 0$. The solid line (Gaussian) is a visual guide.

A. Response of $MoTe_2$ monolayers through strain-induced H → T′ transformations

Stress-strain curves for $MoTe_2$ monolayers under various applied strains are shown in Fig. 7(a). The H crystal exhibits a linear elastic response prior to the onset of T′ domain nucleation. A second linear regime, with smaller effective elastic modulus occurs when T′ domains begin to nucleate and relieve some portion of the applied strain. The amount

of strain relieved and therefore the effective modulus are controlled by the energy minimizing domain morphology realized for a given set of boundary conditions and applied strain. When the H → T′ transformation is complete, a third linear regime exhibiting the elastic modulus of the T′ phase begins.

The interesting aspect of this response is the wide and systematic variation of the effective elastic modulus during H/T′ coexistence as a function of the nature of the applied strain; this is potentially useful in electromechanical applications. To characterize and analyze this effective anisotropy, we first generalize the ways in which strain can be applied and then present results for a number of specific cases.

The space of realizable applied strains can be reduced to two variables that represent the angle of the laboratory frame relative to the H-phase a axis (ϕ_L) and the angle of the strain path taken within a specified laboratory frame [$\phi_P = \arctan(\bar{\epsilon}_{yy}/\bar{\epsilon}_{xx})$, where $\bar{\epsilon}_{ij}$ is defined within the laboratory frame ϕ_L]. Effective H/T′ coexistence moduli $E_{H/T'}$ versus ϕ_P obtained from simulations at $\phi_L = 0$ are shown in Fig. 7(b). The modulus varies periodically between $0 \lesssim E_{H/T'} \lesssim 2E_H/3$ and is near zero through most of quadrants II, III, and IV where the applied strain is compressive in one or both directions.

B. Response of fixed area T′-WTe_2 monolayers

WTe_2 monolayers exhibit a thermodynamically stable T′ phase at zero strain and have been predicted to possess ferroelastic and possibly shape memory properties [8]. This makes WTe_2 an interesting system for studies of mechanical response, as a wide range of its stress-strain behavior will be mediated by rapid rearrangements of its three-variant-orientation T′ microstructure. The microstructure selects the variants and morphologies that best relieve a given applied strain, and the local variant structure can be repeatedly switched without introducing defects. The energy barrier for this switching is very low, ∼0.2 eV/MX_2 [8]. In the absence of significant plasticity associated with mobile defects such as dislocations, the stress-strain response can therefore remain reversible to high applied stresses or strains. The ability to relieve strain through out-of-plane bending also leads to interesting effects.

Using $MoTe_2$ and MoS_2 as guides, the small T′/T′ interfacial energies indicates that elastic rather than interfacial energy minimization will be the primary determinant of microstructure and response during straining for T′ domain sizes larger than ∼10 nm (see Figs. 3 and 11). Simulations in the elasticity-dominated rather than interfacial energy-dominated parameter regimes are therefore appropriate. Even for small domain sizes, inclusion of interfacial anisotropy effects do not qualitatively alter our results because T′/T′ interfacial energies generally favor the same inclinations as the elastic misfit energy, as shown in Sec. III B. We therefore conducted WTe_2 straining in isotropic interface simulations.

Multivariant T′ microstructures were first generated by initializing each freely suspended monolayer with a homogeneous, stress-free H phase and allowing T′ domains to spontaneously nucleate and grow [Fig. 8(a)]. H → T′ transformation leads to buckling wherever the local induced axial stresses are sufficiently negative. The average stresses in the system were relaxed to steady values near zero, then the monolayer was strained uniformly along $\phi_P = 0°, 45°$, or 90° at a low (quasistatic) rate.

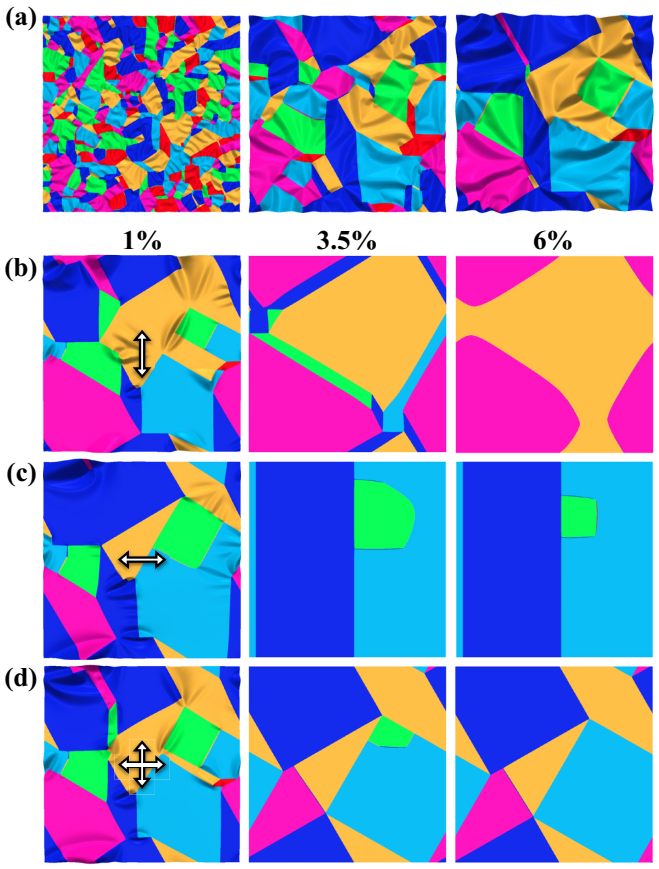

FIG. 8. Domain morphologies of multivariant, freely suspended T′-WTe_2 monolayers under strain. Evolution of T′ variant domains and wrinkles with time (left to right) in (a) an unstrained fixed area monolayer initialized as a single H crystal, and the final state from (a) subjected to strain applied at constant rate along (b) $\phi_P = 90°$, (c) 0°, and (d) 45°. $w(\vec{r})$ is amplified by 5X for visualization.

Our primary findings are summarized in Figs. 8 and 9. Inspection of Fig. 8(a) reveals that the primary T′ domain symmetries observed in flat monolayers (nested threefold stars, fourfold domain wall junctions, and multicomposite wedges/fans) [10] are far less prominent in bendable monolayers. This results from local wrinkle-mediated relief of transformation strain which tends to break the threefold symmetry of local strain states (e.g., when wrinkle pattern symmetries do not match domain symmetries) and generate qualitatively different, less symmetric T′ domain patterns.

A transient kinetic regime exists in which this symmetry reduction is not observed, but the asymptotic state appears to be that with lower T′ domain symmetry. Starting from a flat H monolayer, there are separate driving forces for T′ domain formation and subsequent wrinkle formation, as well as separate factors controlling the kinetics of each. If the initial driving force for wrinkling is sufficiently large (e.g., κ is relatively large), then wrinkle morphologies with larger characteristic lengths than those of T′ domain morphologies will initially develop. During this stage the T′ domain symmetries of flat

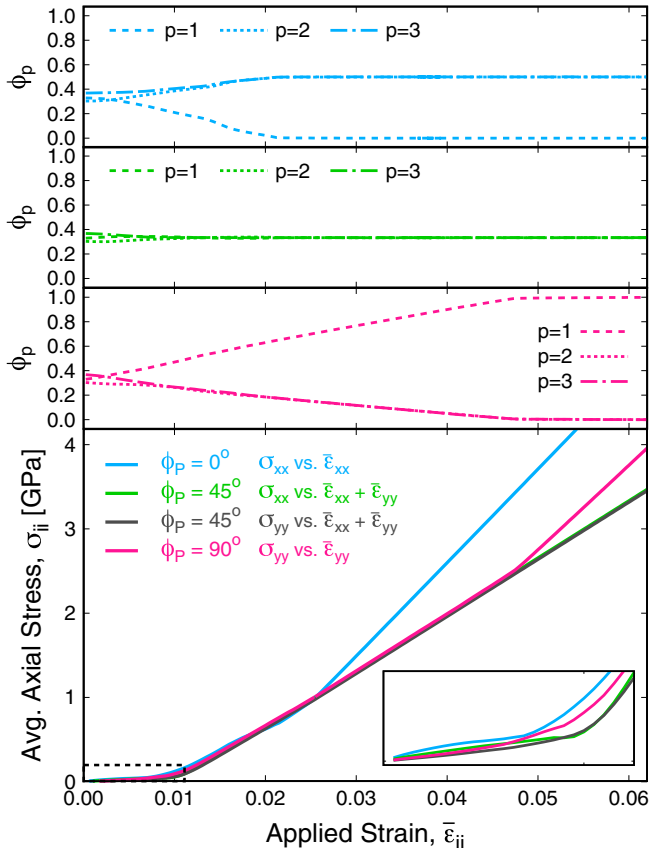

FIG. 9. Mechanical response of multivariant, freely suspended T′-WTe_2 monolayers. Stress-strain curves at $\phi_P = 0^\circ$, 45°, and 90° (lower) and corresponding variations in area fraction of T′ variants (upper three plots). An expanded view of the highlighted low strain region is shown in the lower inset.

monolayers will be observed because the relative wrinkle size is too large to locally alter strain states at junctions. Wrinkles form a coarse wave pattern that essentially overlays the sheet and does not couple strongly to the finely-patterned T′ microstructure.

However, the kinetics of wrinkle coarsening is generally slower than that of domain coarsening, such that even in the scenario above, T′ domains will eventually coarsen to and potentially beyond the typical wrinkle length scale. When this occurs, wrinkle and T′ domain kinetics become more strongly coupled and the wrinkle morphology breaks the threefold T′ domain symmetries, generating a morphology like that of Fig. 8(a). Wrinkles can therefore play a large role in determining the microstructure of T′ monolayers; they eventually become embedded within and across T′ domains and are then an integral part of the morphology rather than a large wavelength overlay. Microstructural rearrangement must involve wrinkle pattern rearrangement in this regime.

In our simulations the wave speeds α_p and α_w are set to be equal. The kinetics of T′ domains and wrinkles are therefore preset to occur on similar time scales. Simulations reveal that the transient kinetic regime with high T′ domain symmetry is observed when κ is sufficiently large, but the asymptotic lower symmetry morphologies emerge with time. The strength of coupling to a substrate can again be employed here to induce changes between the less symmetric T′ domain patterns associated with wrinkles and the more symmetric patterns observed when wrinkling is suppressed.

Upon straining a terminal state such as that shown in Fig. 8(a), either two or three linear stress-strain response regimes are observed, depending on the value of ϕ_P. For $\phi_P = 90^\circ$ [Fig. 8(b)], the effective modulus increases from ∼5 GPa to ∼62 GPa to ∼95 GPa for $0 \leqslant \bar{\epsilon}_{yy} \lesssim 1\%$ (regime I), $1\% \lesssim \bar{\epsilon}_{yy} \lesssim 6.2\%$ (regime II) and $\bar{\epsilon}_{yy} \gtrsim 6.2\%$ (regime III), respectively. In regime I, the wrinkles induced by the initial H → T′ transformation provide "slack" that allows stretching of the monolayer with little elastic energy cost. In regime II, the wrinkles have been "stretched away" and the three-variant microstructure evolves to eliminate variants $p = 2$ and $p = 3$, which do not relieve $\bar{\epsilon}_{yy}$ as effectively as variant $p = 1$. This microstructural evolution or variant switching relieves some fraction of the applied elastic energy. In regime III, variants $p = 2$ and $p = 3$ have been eliminated and the monolayer deforms as a homogeneous elastic sheet with the moduli of the univariant T′ phase, without significant further microstructural evolution.

The response at $\phi_P = 0^\circ$ [Fig. 8(c)] is qualitatively similar to that of $\phi_P = 90^\circ$, except that only the $p = 1$ variant is eliminated during regime II, which terminates at $\bar{\epsilon}_{xx} \approx 2.4\%$. The final microstructure contains a lamellar pattern of variants $p = 2$ and $p = 3$. In the case of $\phi_P = 45^\circ$ [Fig. 8(d)], regime II does not occur because the applied strain favors all three variants equally; none are eliminated. Once the wrinkles are removed, the threefold microstructural symmetry is restored.

V. CONCLUSIONS

Strain and phase engineered multiphase H/T′ TMD monolayers provide a platform for dynamic localized switching between semiconducting H and metallic or semimetallic T′ phases. Exploitation of this transformation in experiments and devices relies on the ability to predict and control T′ and H domain patterns. We have quantitatively characterized domain morphologies and the mechanical response of such monolayers using a combination of first principles and continuum calculations. T′0T′ domains are generally found to be rhombi of fixed proportions, while T′60T′ domains are nearly rectangular with monotonically increasing aspect ratio A_R as a function of domain size L_0. H0T′ domains undergo a morphological change from compact to elongated shapes at $L_0 \approx$ 100–200 nm in flat sheets (bonded to substrates) and $L_0 \gtrsim 2\ \mu$m in bendable (freestanding) sheets.

T′60T′ and H0T′ domain elongation results from elastic misfit energy dominance over interfacial energy with increasing domain size L_0. A general scaling relation $A_R \sim L_0^{2/3}$ is derived from energy balance considerations and verified in the large L_0 limit (above L_0^*). L_0^* is much larger in freely suspended monolayers because much of the in-plane elastic transformation strain energy is relieved through buckling, at the expense of very small bending energy increases. The crossover size L_0^* and therefore T′ domain morphology in partially-transformed monolayers can be tuned via the monolayer-substrate interaction strength. Such control directly facilitates the use of 2D TMDs in experiments and

devices that require the realization of domain patterns with specific geometric and/or morphological features and length scales.

Applied strain can drive the H → T′ transformation, leading to multiregime stress-strain response that is sensitive to the orientation of the applied load. The strain required to induce and complete the transformation also varies significantly with this orientation [10]. These properties could be utilized in electromechanical functions such as multifunctional switches that involve directed uniaxial strains.

Localized buckling in freely suspended, fixed area WTe_2 monolayers following H → T′ transformation is shown to result in qualitatively different T′ domain symmetries than those of flat T′ monolayers. Ferroelastic T′-WTe_2 sheets exhibit either two to three regimes of reversible mechanical response with increasing strain, depending on strain orientation. This anisotropy and systematic variation in elastic moduli with strain provides novel electromechanical functions.

The ability to controllably tune phase morphologies and strain states provides interesting opportunities for fundamental studies and applications involving 2D materials. The study of topologically protected edge states in large-gap quantum spin Hall insulating T′ TMDs [13] and their exploitation in devices relies on the realization of particular interface misorientations and inclinations between neighboring H or T′ domains [14]. The morphologies outlined here and their dependence on domain size and wrinkle state provide guidelines for systematically generating various types of H/T′ and T′/T′ domains and interfaces. Extension of these concepts to electrostatically-induced transformations [9,11,12] could prove particularly effective in a variety of applications, including phase change memory [7,9], advanced electronic devices [15], hydrogen evolution catalysis [16], and Ohmic contacts [17–19].

ACKNOWLEDGMENTS

This work was supported in its entirety as part of the Center for the Computational Design of Functional Layered Materials, an Energy Frontier Research Center funded by the U.S. Department of Energy (DOE), Office of Science, Basic Energy Sciences (BES) under Award DE-SC0012575.

APPENDIX A: DERIVATION OF MESOSCALE GOVERNING EQUATIONS FOR A STRUCTURALLY HETEROGENEOUS, BENDABLE 2D MONOLAYER

Here the elastic energy functional of a structurally heterogeneous, elastically homogeneous, bendable 2D sheet is derived following the approach of Khachaturyan *et al.* [31]. The new element in our derivation is the incorporation of out-of-plane bending within a 2D sheet geometry.

Three starting assumptions are made: (1) all phases have the same elastic moduli, (2) the average length of inclusions and their spacing are both small relative to the total body size, (3) external boundaries of the body are stress free. The calculation is then divided into six steps:

(1) Cut the (arbitrary) shapes of a group of inclusions out of an initially homogeneous parent phase. Assume the inclusions are large enough to ignore any surface energies introduced.

(2) Transform the cutout inclusions to the new phase under stress-free conditions, such that no strain energy is yet introduced. The stress-free transformation strain tensors $\epsilon^0_{ij}(p)$ describe the strains introduced.

(3) Apply surface traction to each inclusion to restore its original shape, introducing the homogeneous strain and stress tensors, $\epsilon_{ij} = -\epsilon^0_{ij}(p)$ and $\sigma_{ij} = -\lambda_{ijkl}\epsilon^0_{ij}(p)$, respectively. The associated elastic energy within one inclusion is

$$\Delta E_{\text{self}}(p) = \tfrac{1}{2} a_p \lambda_{ijkl}\epsilon^0_{ij}(p)\epsilon^0_{kl}(p), \tag{A1}$$

where a_p is the inclusion's area. The total energy change of all inclusions is

$$\Delta E_3 = \frac{1}{2}\sum_p A_p \lambda_{ijkl}\epsilon^0_{ij}(p)\epsilon^0_{kl}(p), \tag{A2}$$

where A_p is the total area of pth type inclusions.

(4) Put the inclusions back into the parent crystal, introducing no energy change at this stage as they are not yet allowed to relax.

(5) "Weld" the inclusions into the parent phase, assuming that coherent interfaces can be established.

(6) Let the inclusions relax, introducing elastic relaxation energy. Write this energy as a power series in the local deformation tensor $\epsilon_{ij}(\vec{r})$, truncated after the second term, and include the out-of-plane bending energy:

$$\Delta E_{\text{R}} = \int_A \Big\{ -\sigma^0_{ij}(\vec{r})\epsilon_{ij} + \frac{1}{2}\lambda_{ijkl}\epsilon_{ij}\epsilon_{kl} + \frac{\kappa}{2}[\nabla^2 w(\vec{r})]^2 + \kappa(1-\nu)[(w(\vec{r})_{,xy})^2 - w(\vec{r})_{,xx}w(\vec{r})_{,yy}]\Big\} dA. \tag{A3}$$

Here A is the area of the sheet, $\sigma^0_{ij}(\vec{r})$ the first order expansion coefficient, which will be defined later, κ is the bending rigidity, ν is the Poisson ratio, and $w(\vec{r})$ is the out-of-plane displacement field, defined relative to the flat sheet at $z = 0$.

The total elastic strain energy must then be determined from the general expressions above. We have

$$E_{\text{elas}} = \Delta E_3 + \Delta E_{\text{R}} = \frac{1}{2}\sum_p A_p \lambda_{ijkl}\epsilon^0_{ij}(p)\epsilon^0_{kl}(p) + \int_A \Big\{ -\sigma^0_{ij}(\vec{r})\epsilon_{ij} + \frac{1}{2}\lambda_{ijkl}\epsilon_{ij}\epsilon_{kl} + \frac{\kappa}{2}[\nabla^2 w(\vec{r})]^2 + \kappa(1-\nu)[(w(\vec{r})_{,xy})^2 - w(\vec{r})_{,xx}w(\vec{r})_{,yy}]\Big\} dA. \tag{A4}$$

The linear term in the integral does not vanish because the system is structurally heterogeneous and is therefore strained in the stress-free state [$\epsilon_{ij}(\vec{r}) \neq 0$ when $\sigma_{ij}(\vec{r}) = 0$]. The strain tensor of the stress-free state is therefore

$$\epsilon^0_{ij}(\vec{r}) = \sum_{p=1}^{v} \Theta_p(\vec{r})\epsilon^0_{ij}(p), \tag{A5}$$

where $\Theta_p(\vec{r})$ is the shape function of p-type inclusions, equal to 1 inside a p-type inclusion and 0 otherwise, and v is the number of inclusion types or orientations.

The elastic stress can be obtained from

$$\sigma_{ij}(\vec{r}) = \frac{\delta E_{\text{elas}}}{\delta \epsilon_{ij}(\vec{r})} = -\sigma^0_{ij}(\vec{r}) + \lambda_{ijkl}\epsilon_{kl}. \tag{A6}$$

In the stress-free state $\sigma_{ij}(\vec{r}) = 0$ and $\epsilon_{ij}(\vec{r}) = \epsilon^0_{ij}(\vec{r})$, implying that

$$\sigma^0_{ij}(\vec{r}) = \lambda_{ijkl}\epsilon^0_{kl}(\vec{r}) = \lambda_{ijkl}\sum_{p=1}^{v}\Theta_p(\vec{r})\epsilon^0_{kl}(p) = \sum_{p=1}^{v}\sigma^0_{ij}(p)\Theta_p(\vec{r}), \tag{A7}$$

where $\sigma^0_{ij}(p) = \lambda_{ijkl}\epsilon^0_{kl}(p)$. This defines the first order expansion coefficient from step 6, giving

$$\Delta E_{\text{R}} = \int_A \left\{ -\sum_{p=1}^{v}\sigma^0_{ij}(p)\Theta_p(\vec{r})\epsilon_{ij} + \frac{1}{2}\lambda_{ijkl}\epsilon_{ij}\epsilon_{kl} + \frac{\kappa}{2}[\nabla^2 w(\vec{r})]^2 + \kappa(1-\nu)[(w(\vec{r})_{,xy})^2 - w(\vec{r})_{,xx}w(\vec{r})_{,yy}]\right\} dA. \tag{A8}$$

To obtain a functional of phase field order parameters $\eta_p(\vec{r})$, the binary shape functions $\Theta_p(\vec{r})$ can be written as a power series in $\eta_p(\vec{r})$. We assume that the energy is invariant under $\eta_p \to -\eta_p$, such that the linear term in the expansion must vanish by symmetry. Then to second order,

$$\epsilon^0_{ij}(\vec{r}) = \sum_{p=1}^{v}\Theta_p(\vec{r})\epsilon^0_{ij}(p) = \sum_{p=1}^{v}\eta^2_p(\vec{r})\epsilon^0_{ij}(p). \tag{A9}$$

If η_p is assumed to be normalized to $[-1, 1]$, then the total elastic energy is

$$E_{\text{elas}} = \Delta E_3 + \Delta E_{\text{R}} = \frac{1}{2}\int_A \sum_p \sum_q \left[\lambda_{ijkl}\epsilon^0_{ij}(p)\epsilon^0_{kl}(q)\eta^2_p(\vec{r})\eta^2_q(\vec{r})\right] dA + \int_A \left\{ -\sum_{p=1}^{3}\lambda_{ijkl}\epsilon^0_{kl}(p)\eta^2_p(\vec{r})\epsilon_{ij}(\vec{r}) \right.$$
$$\left. + \frac{1}{2}\lambda_{ijkl}\epsilon_{ij}(\vec{r})\epsilon_{kl}(\vec{r}) + \frac{\kappa}{2}[\nabla^2 w(\vec{r})]^2 + \kappa(1-\nu)[(w(\vec{r})_{,xy})^2 - w(\vec{r})_{,xx}w(\vec{r})_{,yy}]\right\} dA. \tag{A10}$$

The strain tensor is now introduced and is taken to be linear in the local in-plane displacements $u_i(\vec{r})$ and second order in the local out-of-plane displacements $w(\vec{r})$,

$$\epsilon_{ij}(\vec{r}) = \bar{\epsilon}_{ij} + \delta\epsilon_{ij}(\vec{r}) = \bar{\epsilon}_{ij} + \tfrac{1}{2}(u_{i,j} + u_{j,i} + w_{,i}w_{,j}). \tag{A11}$$

This form is appropriate for moderately large out-of-plane deformations. $\bar{\epsilon}_{ij}$ is the uniform macroscopic strain due to the inclusions (or an applied macroscopic strain), and $\delta\epsilon_{ij}(\vec{r})$ contains heterogeneous strains which have no net macroscopic effect. With this definition, the elastic strain energy becomes

$$E_{\text{elas}} = \Delta E_3 + \Delta E_{\text{R}} \qquad \Delta E_3 = \frac{1}{2}\int_A \sum_p \sum_q \left[\lambda_{ijkl}\epsilon^0_{ij}(p)\epsilon^0_{kl}(q)\eta^2_p(\vec{r})\eta^2_q(\vec{r})\right] dA \qquad \Delta E_{\text{R}} = E^{\text{hom}}_{\text{R}} + E^{\text{het}}_{\text{R}}$$

$$E^{\text{hom}}_{\text{R}} = -\int_A \sum_p \left[\lambda_{ijkl}\bar{\epsilon}_{ij}\epsilon^0_{kl}(p)\eta^2_p(\vec{r})\right] dA + \frac{A}{2}\lambda_{ijkl}\bar{\epsilon}_{ij}\bar{\epsilon}_{kl}$$

$$E^{\text{het}}_{\text{R}} = \int_A \left\{ -\sum_{p=1}^{v}\lambda_{ijkl}\epsilon^0_{kl}(p)\eta^2_p(\vec{r})\frac{1}{2}(u_{i,j} + u_{j,i} + w_{,i}w_{,j}) + \frac{\kappa}{2}[\nabla^2 w(\vec{r})]^2 + \kappa(1-\nu)[(w(\vec{r})_{,xy})^2 - w(\vec{r})_{,xx}w(\vec{r})_{,yy}] \right.$$
$$\left. + \frac{1}{2}\lambda_{ijkl}\left[\frac{1}{2}(u_{i,j} + u_{j,i} + w_{,i}w_{,j})\frac{1}{2}(u_{k,l} + u_{l,k} + w_{,k}w_{,l}) + \frac{1}{2}(\bar{\epsilon}_{ij}w_{,k}w_{,l} + \bar{\epsilon}_{kl}w_{,i}w_{,j})\right]\right\} dA. \tag{A12}$$

In this form the elastic strain energy depends on four sets of internal parameters:

(1) the macroscopic homogeneous strains $\bar{\epsilon}_{ij}$,
(2) the local in-plane displacements $u_x(\vec{r})$ and $u_y(\vec{r})$,
(3) the local out-of-plane displacement $w(\vec{r})$, and
(4) the local order parameter variants $\eta_p(\vec{r})$.

The corresponding conditions of mechanical equilibrium are

$$\frac{\partial E_{\text{elas}}}{\partial \bar{\epsilon}_{ij}} = 0 \quad \frac{\partial E_{\text{elas}}}{\partial u_i(\vec{r})} = 0 \quad \frac{\partial E_{\text{elas}}}{\partial w(\vec{r})} = 0 \quad \frac{\partial E_{\text{elas}}}{\partial \eta_p(\vec{r})} = 0. \tag{A13}$$

In the $w(\vec{r}) = 0$ case, Khachaturyan *et al.* use the corresponding equations to derive explicit analytic solutions for $\bar{\epsilon}_{ij}$ and $u_i(\vec{r})$ in terms of $\epsilon^0_{ij}(p)$ and $\eta_p(\vec{r})$. The conditions of mechanical equilibrium can then be explicitly formulated in terms of a single closed equation for each $\eta_p(\vec{r})$. This approach cannot be directly adapted to the highly nonlinear $w(\vec{r}) \neq 0$ case. We therefore derive the equilibrium equation of each parameter while holding all other parameters fixed and solve the resulting set of equations with a combined analytical/numerical approach outlined in Ref. [10]. In all that follows, the second bending energy term in Eq. (7), that multiplied by $(1-\nu)$, will be set to zero, its value when the boundaries of the plate are clamped.

1. Equilibrium w.r.t. macroscopic homogeneous strains

When the macroscopic homogeneous strains $\bar{\epsilon}_{ij}$ are not fixed by strain-controlled boundary conditions, mechanical equilibrium is realized at

$$\frac{\partial E_{\text{elas}}}{\partial \bar{\epsilon}_{ij}} = -\int_A \sum_{p=1}^{v} \left[\lambda_{ijkl}\epsilon^0_{kl}(p)\eta_p^2(\vec{r})\right] dA + A\lambda_{ijkl}\bar{\epsilon}_{kl} + \int_A \frac{1}{2}\lambda_{ijkl} w_{,k} w_{,l} dA = 0 \tag{A14}$$

or

$$\bar{\epsilon}_{ij} = \frac{1}{A}\int_A \left[\sum_{p=1}^{v} \epsilon^0_{kl}(p)\eta_p^2(\vec{r}) - \frac{1}{2} w_{,k} w_{,l}\right] dA. \tag{A15}$$

The solution for the homogeneous relaxation energy in this case is given by substituting this result into Eq. (A12). When the macroscopic homogeneous strains $\bar{\epsilon}_{ij}$ are fixed by strain-controlled boundary conditions, it is not necessary to minimize E_{elas} with respect to $\bar{\epsilon}_{ij}$.

2. Equilibrium w.r.t. in-plane displacements

To compute mechanical equilibrium with respect to $u_i(\vec{r})$,

$$\frac{\partial E_{\text{elas}}}{\partial u_i(\vec{r})} = \frac{\partial \Delta E_{\text{R}}}{\partial u_i(\vec{r})} = 0, \tag{A16}$$

the heterogeneous relaxation energy must be expressed in terms of $u_i(\vec{r})$. This can be done by computing the first variation or differential of ΔE_{R}, employing the symmetries $\sigma^0_{ij}(p) = \sigma^0_{ji}(p)$ and $\lambda_{ijkl} = \lambda_{jikl} = \lambda_{ijlk} = \lambda_{klij}$, and applying the divergence theorem several times. The result is

$$\delta(\Delta E_{\text{R}}) = \int_A \left\{ \sum_{p=1}^{v} \sigma^0_{ij}(p)\left[\left(\eta_p^2(\vec{r})\right)_{,j}(\delta u_i + w_{,i}\delta w) + \eta_p^2(\vec{r}) w_{,ij}\delta w\right] + \kappa(\nabla^4 w(\vec{r}))\delta w - \frac{1}{2}\lambda_{ijkl}\Big[(2u_{k,lj} + w_{,k}w_{,lj} + w_{,l}w_{,kj})\delta u_i + \left(2\frac{\partial}{\partial r_i}(u_{k,l}w_{,j}) + \frac{\partial}{\partial r_i}(w_{,j}w_{,k}w_{,l}) + 2\bar{\epsilon}_{kl}w_{,ji}\right)\delta w\Big]\right\} dA. \tag{A17}$$

The equation of mechanical equilibrium for $u_i(\vec{r})$ is therefore

$$\frac{\delta \Delta E_{\text{R}}}{\delta u_i(\vec{r})} = -\frac{1}{2}\lambda_{ijkl}(2u_{k,lj} + w_{,k}w_{,lj} + w_{,l}w_{,kj}) + \sum_{p=1}^{v} \sigma^0_{ij}(p)\left(\eta_p^2(\vec{r})\right)_{,j} = 0 \tag{A18}$$

or

$$\frac{1}{2}\lambda_{ijkl}(2u_{k,lj} + w_{,k}w_{,lj} + w_{,l}w_{,kj}) = \sum_{p=1}^{v} \sigma^0_{ij}(p)\left(\eta_p^2(\vec{r})\right)_{,j}. \tag{A19}$$

Equation (A19) is linear in $u_i(\vec{r})$ and can therefore be solved analytically to obtain the equilibrium displacements, following largely the standard approach. We first multiply both sides by $e^{-i\vec{k}\vec{r}}$ and integrate over A,

$$\int_A \frac{1}{2}\lambda_{ijkl}(2u_{k,lj} + w_{,k}w_{,lj} + w_{,l}w_{,kj}) e^{-i\vec{k}\vec{r}} dA = \int_A \sum_{p=1}^{v} \sigma^0_{ij}(p)\left(\eta_p^2(\vec{r})\right)_{,j} e^{-i\vec{k}\vec{r}} dA. \tag{A20}$$

This result is equivalent to Eq. (10), and its solution is given by Eq. (14).

3. Equilibrium w.r.t. out-of-plane displacements

The equation of mechanical equilibrium for $w(\vec{r})$, Eq. (11), can be directly obtained from Eq. (A17).

4. Equilibrium w.r.t. order parameter variants

The equation of mechanical equilibrium for the order parameters, Eq. (12), can be obtained directly from Eq. (A12).

APPENDIX B: SIMULATION METHOD WITH INTERFACIAL ANISOTROPY AND CONSERVED AREA KINETICS

For simulations at length scales near or below the morphological crossover scale L_0^*, interfacial anisotropy and η_p conservation (for fixed area T′ domains) were implemented. The convexification approach noted in the main text was employed to handle the technical challenges associated with the large H0T′ interfacial anisotropy and subsequent domain faceting. The technical challenge arises due to the fact that under sufficiently large anisotropy, the equations of motion become ill-posed, backward parabolic equations over certain ranges of unstable inclinations. The convexification method regularizes the equations over the unstable $\hat{\phi}$ values and produces the correct equilibrium domain shapes. Further details of the method can be found in Ref. [51]; here we straightforwardly adapted the original scheme to the case of combined threefold and dual twofold symmetry.

In the simulations associated with Figs. 5 and 6 of the main text, single $p = 1$ T′ domains of various size were initialized either as circles or as rectangles with $\zeta = \phi_{\text{habit}}$ and $A_R = 2$–15. These correspond to infinite arrays of identical domains due to the use of periodic boundary conditions, but

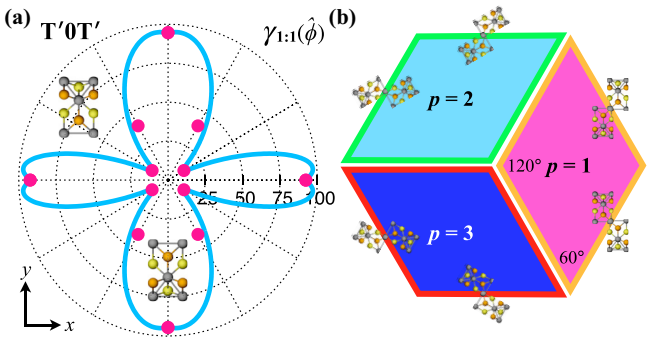

FIG. 10. T′0T′ interfaces and domain morphologies in MoS_2. (a) Anisotropy in interfacial energy $\gamma_{1:1}(\hat{\phi})$ as determined from DFT calculations (points) and the best fit to Eq. (17) (line). Energy units are meV/Å. (b) Equilibrium (sub)domain shapes for each variant orientation p as determined from the Wulff construction employing the best fit to Eq. (17).

results were compared at multiple system sizes to confirm convergence toward the isolated inclusion limit. Relaxation to the energy minimizing shape at fixed domain area was achieved by evolving the order parameters as

$$\frac{\partial \eta_p}{\partial t} = -M_p\left(\frac{\delta \tilde{F}_{\rm tot}}{\delta \eta_p} - \lambda_p\right) + \nu_p, \tag{B1}$$

where M_p is a constant mobility parameter, $\lambda_p = A^{-1}\int_A(\delta \tilde{F}_{\rm tot}/\delta\eta_p)d\vec{r}$ is the Lagrange multiplier that enforces global conservation of η_p, and ν_p is the previously defined Gaussian noise term, in this case of very small magnitude. This evolution equation permits rapid, nondiffusive relaxations toward equilibrium while maintaining global conservation of each η_p.

APPENDIX C: T′ DOMAIN SHAPES IN MoS_2

MoS_2 interfacial energies determined from DFT calculations are presented here in Figs. 10 and 11, along with the computed T′0T′ and T′60T′ domain morphologies. The interfacial energy values were previously reported in Ref. [28]. Results are very similar to those of $MoTe_2$ shown in Figs. 2 and 3.

APPENDIX D: MODIFIED ESHELBY CALCULATION OF T′ DOMAIN SHAPES

Details of the calculation of isolated T′ domain shapes when embedded within the matrix of H phase are outlined here. The aim is to determine the T′ domain size L_0^* at which a crossover from compact to elongated shapes occurs. We write the total energy difference between compact and elongated domain shapes in terms of the elastic ($E_i^{\rm elas}$) and interfacial ($E_i^{\rm int}$) contributions to each,

$$\begin{aligned}\Delta E^{\rm tot} &= E^{\rm tot}_{\rm com} - E^{\rm tot}_{\rm elo}\\ &= E^{\rm elas}_{\rm com} + E^{\rm int}_{\rm com} - E^{\rm elas}_{\rm elo} - E^{\rm int}_{\rm elo}\\ &= E_{0,\rm com}L_0^2/4 + \bar{P}_{\rm com}\bar{\gamma}_{\rm com}L_0\\ &\quad - E_{0,\rm elo}L_0^2/4 - \bar{P}_{\rm elo}\bar{\gamma}_{\rm elo}L_0.\end{aligned} \tag{D1}$$

$E^{\rm tot}_{\rm com}$ and $E^{\rm tot}_{\rm elo}$ are the total interfacial plus elastic misfit energies of the optimized compact and elongated domains, respectively, at a given L_0. The last equality invokes the fact that the elastic energies can be expressed as the product of the inclusion area and a prefactor E_0, to be specified in the following. It also invokes the fact that the total interfacial energy of a domain can be expressed as the product of its perimeter length P_i and a mean interfacial energy $\bar{\gamma}_i$ ($\bar{P}_{\rm com}$ and $\bar{P}_{\rm elo}$ are the domain perimeter lengths scaled relative to L_0).

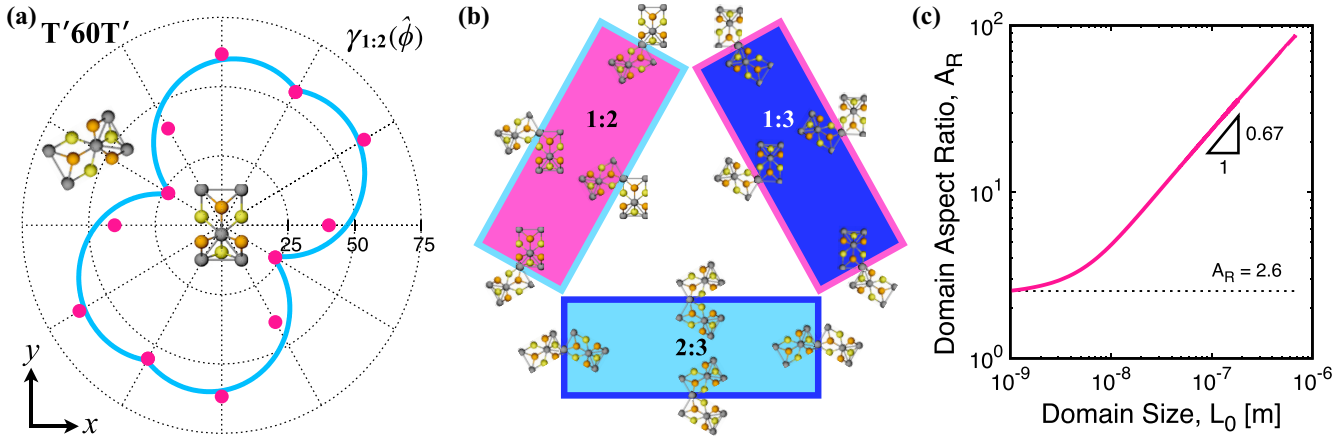

FIG. 11. T′60T′ interfaces and domain morphologies in MoS_2. (a) Anisotropy in interfacial energy $\gamma_{1:2}(\hat{\phi})$ as determined from DFT calculations (points) and the best fit to Eq. (18) (line). Energy units are meV/Å. (b) Equilibrium domain shapes for each variant orientation pair p:q as determined from the Wulff construction employing the best fit to Eq. (18) but neglecting the effect of misfit strain (valid only for very small domain sizes). The possible crystal orientations across each interface are shown for each pair; the inner:outer domains can be p:q or q:p. (c) Equilibrium domain axial ratio A_R increases with domain size L_0, crossing over from interface dominated to elastic misfit dominated A_R behavior above $L_0 \simeq 10$ nm. Results were obtained via the Eshelby misfitting inclusion calculation with anisotropic interfacial energy described in the main text.

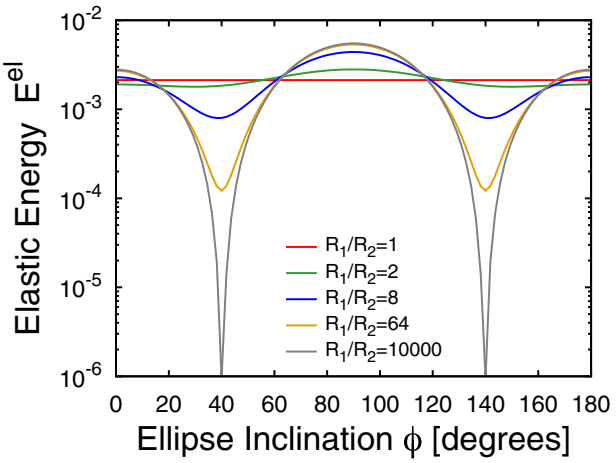

FIG. 12. Elastic energy from Eq. (D5) as a function of ellipse inclination ζ for various aspect ratios. Vanishing of the elastic energy at the habit inclination near $\zeta = 40^\circ$ is apparent at large aspect ratios.

The general solution of $\Delta E^{\rm tot} = 0$ based on Eq. (D1) is given in Eq. (20). The form of this result shows that L_0^* is controlled by the ratio of the differences between the average interfacial energy densities and the total elastic energy densities of the two domain shapes. The interfacial terms in the numerator are determined from DFT computations and the geometric approximations described in the main text. The elastic terms in the denominator are determined using Eshelby's classic analysis of elastically misfitting coherent inclusions. The elastic energy is first specified as

$$E^{\rm el}(R_1, R_2) = -\tfrac{1}{2}\sigma_{ij}^I \epsilon_{ij}^0 A_0 h \tag{D2}$$

$$= -\tfrac{1}{2}\lambda_{ijkl}\left(\epsilon_{kl}^c - \epsilon_{kl}^0\right)\epsilon_{ij}^0 A_0 h, \tag{D3}$$

where A_0 is the inclusion area, and $\sigma_{ij}^I = \lambda_{ijkl}(\epsilon_{kl}^c - \epsilon_{kl}^0)$ and $\epsilon_{ij}^c = S_{ijkl}\epsilon_{kl}^0$ are the relaxational stress and strain, respectively, associated with the inclusion. The task is to solve for the Eshelby tensor S_{ijkl}. Following the standard approach, the result for plane stress is

$$S_{ijkl} = \frac{3\nu - 1}{8}\delta_{ij}\delta_{kl} + \frac{3 - \nu}{8}(\delta_{ik}\delta_{jl} + \delta_{il}\delta_{jk}). \tag{D4}$$

The associated energy for arbitrary inclination ζ and area $A_0 = \pi R_1 R_2 = \pi L_0^2/4$ is $E_{\rm elo}^{\rm elas} = E_0(\zeta, A_R, \epsilon_{ij}^0) R_1 R_2$, where

$$\begin{aligned} &E_0\left(\zeta, A_R, \epsilon_{ij}^0\right) \\ &= \frac{\pi\mu(1+\nu)h}{2}\Bigg[\left(2\frac{R_2^2+2R_1R_2}{(R_1+R_2)^2} - \frac{R_2}{R_1+R_2}\right)\epsilon_{xx}^0(\zeta)\epsilon_{xx}^0(\zeta) \\ &\quad + \left(2 - \frac{R_1^2+2R_1R_2}{(R_1+R_2)^2} - \frac{R_1}{R_1+R_2}\right)\epsilon_{yy}^0(\zeta)\epsilon_{yy}^0(\zeta) \\ &\quad + \frac{2R_1R_2}{(R_1+R_2)^2}\left(\epsilon_{xx}^0(\zeta)\epsilon_{yy}^0(\zeta) + 2\epsilon_{xy}^0(\zeta)\epsilon_{xy}^0(\zeta)\right)\Bigg] \end{aligned} \tag{D5}$$

and $\epsilon_{ij}^0(\zeta) = \mathbf{R}^{\mathbf{T}}[\zeta]\epsilon_{ij}^0\mathbf{R}[\zeta]$. Equation (D5) captures the effect of habit inclination, as shown in Fig. 12.

[1] P. Johari and V. B. Shenoy, Tuning the electronic properties of semiconducting transition metal dichalcogenides by applying mechanical strains, ACS Nano **6**, 5449 (2012).

[2] A. Castellanos-Gomez, R. Roldán, E. Cappelluti, M. Buscema, F. Guinea, H. S. J. van der Zant, and G. A. Steele, Local strain engineering in atomically thin MoS_2, Nano Lett. **13**, 5361 (2013).

[3] D. Voiry, A. Mohite, and M. Chhowalla, Phase engineering of transition metal dichalcogenides, Chem. Soc. Rev. **44**, 2702 (2015).

[4] K.-A. N. Duerloo, Y. Li, and E. J. Reed, Structural phase transitions in two-dimensional Mo- and W-dichalcogenide monolayers, Nat. Commun. **5**, 4214 (2014).

[5] S. Song, D. H. Keum, S. Cho, D. Perello, Y. Kim, and Y. H. Lee, Room temperature semiconductor-metal transition of $MoTe_2$ thin films engineered by strain, Nano Lett. **16**, 188 (2016).

[6] Y.-C. Lin, D. O. Dumcenco, Y.-S. Huang, and K. Suenaga, Atomic mechanism of the semiconducting-to-metallic phase transition in single-layered MoS_2, Nat. Nanotech. **9**, 391 (2014).

[7] K.-A. N. Duerloo and E. J. Reed, Structural phase transitions by design in monolayer alloys, ACS Nano **10**, 289 (2016).

[8] W. Li and J. Li, Ferroelasticity and domain physics in two-dimensional transition metal dichalcogenide monolayers, Nat. Commun. **7**, 10843 (2016).

[9] Y. Li, K.-A. N. Duerloo, K. Wauson, and E. J. Reed, Structural semiconductor-to-semimetal phase transition in two-dimensional materials induced by electrostatic gating, Nat. Commun. **7**, 10671 (2016).

[10] J. Berry, S. Zhou, J. Han, D. J. Srolovitz, and M. P. Haataja, Dynamic phase engineering of bendable transition metal dichalcogenide monolayers, Nano Lett. **17**, 2473 (2017).

[11] Y. Wang, J. Xiao, H. Zhu, Y. Li, Y. Alsaid, K. Y. Fong, Y. Zhou, S. Wang, W. Shi, Y. Wang *et al.*, Structural phase transition in monolayer $MoTe_2$ driven by electrostatic doping, Nature (London) **550**, 487 (2017).

[12] D. A. Rehn, Y. Li, E. Pop, and E. J. Reed, Theoretical potential for low energy consumption phase change memory utilizing electrostatically-induced structural phase transitions in 2D materials, npj Comput. Mater. **4**, 2 (2018).

[13] X. Qian, J. Liu, L. Fu, and J. Li, Quantum spin Hall effect in two-dimensional transition metal dichalcogenides, Science **346**, 1344 (2014).

[14] M. M. Ugeda, A. Pulkin, S. Tang, H. Ryu, Q. Wu, Y. Zhang, D. Wong, Z. Pedramrazi, A. Martín-Recio1, Y. Chen, F. Wang, Z.-X. Shen, S.-K. Mo, O. V. Yazyev, and M. F. Crommie, Observation of topologically protected states at crystalline phase boundaries in single-layer WSe_2, arXiv:1802.01339.

[15] G. Eda, T. Fujita, H. Yamaguchi, D. Voiry, M. Chen, and M. Chhowalla, Coherent atomic and electronic heterostructures of single-layer MoS_2, ACS Nano **6**, 7311 (2012).

[16] D. Voiry, H. Yamaguchi, J. Li, R. Silva, D. C. Alves, T. Fujita, M. Chen, T. Asefa, V. B. Shenoy, G. Eda, and M. Chhowalla, Enhanced catalytic activity in strained chemically exfoliated

WS_2 nanosheets for hydrogen evolution, Nat. Mater. **12**, 850 (2013).

[17] R. Kappera, D. Voiry, S. E. Yalcin, B. Branch, G. Gupta, A. D. Mohite, and M. Chhowalla, Phase-engineered low-resistance contacts for ultrathin MoS_2 transistors, Nat. Mater. **13**, 1128 (2014).

[18] A. Allain, J. Kang, K. Banerjee, and A. Kis, Electrical contacts to two-dimensional semiconductors, Nat. Mater. **14**, 1195 (2015).

[19] S. Cho, S. Kim, J. H. Kim, J. Zhao, J. Seok, D. H. Keum, J. Baik, D.-H. Choe, K. J. Chang, K. Suenaga, S. W. Kim, Y. H. Lee, and H. Yang, Phase patterning for ohmic homojunction contact in $MoTe_2$, Science **349**, 625 (2015).

[20] M. Calandra, Chemically exfoliated single-layer MoS_2: Stability, lattice dynamics, and catalytic adsorption from first principles, Phys. Rev. B **88**, 245428 (2013).

[21] M. Kan, J. Wang, X. Li, S. Zhang, Y. Li, Y. Kawazoe, Q. Sun, and P. Jena, Structures and phase transition of a MoS_2 monolayer, J. Phys. Chem. C **118**, 1515 (2014).

[22] T. A. Empante, Y. Zhou, V. Klee, A. E. Nguyen, I.-H. Lu, M. D. Valentin, S. A. Naghibi Alvillar, E. Preciado, A. J. Berges, C. S. Merida, M. Gomez, S. Bobek, M. Isarraraz, E. J. Reed, and L. Bartels, Chemical vapor deposition growth of few-layer $MoTe_2$ in the 2H, 1T′ and 1T phases: Tunable properties of $MoTe_2$ films, ACS Nano **11**, 900 (2017).

[23] G. Kresse and J. Furthmüller, Efficiency of ab-initio total energy calculations for metals and semiconductors using a plane-wave basis set, Comput. Mater. Sci. **6**, 15 (1996).

[24] G. Kresse and J. Furthmüller, Efficient iterative schemes for ab initio total-energy calculations using a plane-wave basis set, Phys. Rev. B **54**, 11169 (1996).

[25] P. E. Blöchl, Projector augmented-wave method, Phys. Rev. B **50**, 17953 (1994).

[26] J. P. Perdew, J. Chevary, S. Vosko, K. A. Jackson, M. R. Pederson, D. Singh, and C. Fiolhais, Atoms, molecules, solids, and surfaces: Applications of the generalized gradient approximation for exchange and correlation, Phys. Rev. B **46**, 6671 (1992).

[27] J. P. Perdew, K. Burke, and M. Ernzerhof, Generalized Gradient Approximation Made Simple, Phys. Rev. Lett. **77**, 3865 (1996).

[28] S. Zhou, J. Han, J. Sun, and D. J. Srolovitz, MoS_2 edges and heterophase interfaces: energy, structure and phase engineering, 2D Materials **4**, 025080 (2017).

[29] Y. Wang and A. Khachaturyan, Three-dimensional field model and computer modeling of martensitic transformations, Acta Mater. **45**, 759 (1997).

[30] Y. Wang and A. G. Khachaturyan, Multi-scale phase field approach to martensitic transformations, Mater. Sci. Eng.: A **438-440**, 55 (2006).

[31] A. Khachaturyan, *Theory of Structural Transformations in Solids* (Dover Publications, Mineola, NY, 2013).

[32] L. Landau and E. Lifshitz, *Theory of Elasticity, Third Edition* (Elsevier, Amsterdam, 2008).

[33] Y. Wen, Y. Wang, and L.-Q. Chen, Effect of elastic interaction on the formation of a complex multi-domain microstructural pattern during a coherent hexagonal to orthorhombic transformation, Acta Mater. **47**, 4375 (1999).

[34] Y. Wen, Y. Wang, and L.-Q. Chen, Phase-field simulation of domain structure evolution during a coherent hexagonal-to-orthorhombic transformation, Philos. Mag. A **80**, 1967 (2000).

[35] Y. Wen, Y. Wang, and L.-Q. Chen, Influence of an applied strain field on microstructural evolution during the $\alpha_2 \rightarrow O$-phase transformation in Ti-Al-Nb system, Acta Mater. **49**, 13 (2001).

[36] Y. Wen, Y. Wang, and L.-Q. Chen, Coarsening dynamics of self-accommodating coherent patterns, Acta Mater. **50**, 13 (2002).

[37] R. C. Cooper, C. Lee, C. A. Marianetti, X. Wei, J. Hone, and J. W. Kysar, Nonlinear elastic behavior of two-dimensional molybdenum disulfide, Phys. Rev. B **87**, 035423 (2013).

[38] Z. Fan, Z. Wei-Bing, and T. Bi-Yu, Electronic structures and elastic properties of monolayer and bilayer transition metal dichalcogenides MX_2 (M = Mo, W; X = O, S, Se, Te): a comparative first-principles study, Chin. Phys. B **24**, 097103 (2015).

[39] B. Mortazavi, G. R. Berdiyorov, M. Makaremi, and T. Rabczuk, Mechanical responses of two-dimensional $MoTe_2$; pristine 2H, 1T and 1T′ and 1T′/2H heterostructure, Extreme Mech. Lett. **20**, 65 (2018).

[40] N. T. Hung, A. R. Nugraha, and R. Saito, Two-dimensional MoS_2 electromechanical actuators, J. Phys. D **51**, 075306 (2018).

[41] E. Torun, H. Sahin, S. Cahangirov, A. Rubio, and F. Peeters, Anisotropic electronic, mechanical, and optical properties of monolayer WTe_2, J. Appl. Phys. **119**, 074307 (2016).

[42] P. Galenko, Phase-field model with relaxation of the diffusion flux in nonequilibrium solidification of a binary system, Phys. Lett. A **287**, 190 (2001).

[43] T. Koide, G. Krein, and R. O. Ramos, Incorporating memory effects in phase separation processes, Phys. Lett. B **636**, 96 (2006).

[44] A. J. Archer, Dynamical density functional theory for dense atomic liquids, J. Phys.: Condens. Matter **18**, 5617 (2006).

[45] P. Stefanovic, M. Haataja, and N. Provatas, Phase-Field Crystals with Elastic Interactions, Phys. Rev. Lett. **96**, 225504 (2006).

[46] S. Majaniemi and M. Grant, Dissipative phenomena and acoustic phonons in isothermal crystals: A density-functional theory study, Phys. Rev. B **75**, 054301 (2007).

[47] A. Molina-Sánchez and L. Wirtz, Phonons in single-layer and few-layer MoS_2 and WS_2, Phys. Rev. B **84**, 155413 (2011).

[48] Though the ZA phonon dispersions of TMD monolayers have the form [47] $\omega_{ZA} \approx Ak^2$ rather than the linear form of LA and TA phonons ($\omega_{LA} \approx \alpha_{LA}k$ and $\omega_{TA} \approx \alpha_{TA}k$), ω_{ZA} can be approximated as linear in k for k sufficiently small. The ZA wave speed employed in the main text corresponds to the linear fit for $k < \pi/(8a)$ or $\lambda > 16a$.

[49] Y. Cai, J. Lan, G. Zhang, and Y.-W. Zhang, Lattice vibrational modes and phonon thermal conductivity of monolayer MoS_2, Phys. Rev. B **89**, 035438 (2014).

[50] D. Cakır, F. M. Peeters, and C. Sevik, Mechanical and thermal properties of h-MX2 (M = Cr, Mo, W; X = O, S, Se, Te) monolayers: A comparative study, Appl. Phys. Lett. **104**, 203110 (2014).

[51] J. Eggleston, G. McFadden, and P. Voorhees, A phase-field model for highly anisotropic interfacial energy, Physica D: Nonlinear Phenomena **150**, 91 (2001).